Optical Enhancement via Electrode Designs for High-Performance Polymer Solar Cells

*Chu-Chen Chueh, Michael Crump, and Alex K.-Y. Jen**

To capture the essence of the rapid progress in optical engineering exploited in high-performance polymer solar cells (PSCs), a comprehensive overview focusing on recent developments and achievements in PSC electrode engineering is provided in this review. To date, various kinds of electrode materials and geometries are exploited to enhance light-trapping in devices through distinct optical strategies. In addition to the widely used nanostructured electrodes that induce plasmonic-enhanced light absorption, planar ultra-thin metal films also have attracted significant attention due to their remarkably reflective transparent properties that beget efficient optical microcavities. These microcavities confine incident light with resonant frequencies between two reflective electrodes due to optically coherent interference, boosting the light absorption of thin-film PSCs while maintaining efficient charge dissociation and extraction. After reviewing the challenges in developing high-performance microcavity-enhanced PSCs (MCPSCs), we discuss strategies to improve MCPSC performance further to showcase the potential of harnessing microcavity resonance effects in thin-film PSCs.

1. Introduction

Inexpensive and lightweight polymer solar cells (PSCs) have attracted considerable research interest in the past decade due to their flexibility and low-temperature solution processability. These inherent advantages make PSCs more compatible for scalable roll-to-roll fabrication than their inorganic counterparts.[1] Thus far, power conversion efficiencies (PCEs) greater than 10% have been realized in bulk-heterojunction (BHJ) PSCs, demonstrating the promising potential of PSCs for future large-scale commercialization.[2–5]

To develop high-performance PSCs, the most critical challenge lies in the incomplete absorption of incident light arising from thin photoactive layers (≈100–180 nm). The intrinsically high exciton binding energy, short exciton diffusion length, and low carrier mobility of organic semiconductors necessitate thin organic absorbing layers to achieve efficient charge dissociation and transport in devices.[6–8] Severe charge recombination that decreases the fill factor (FF) of PSCs becomes more prevalent as the thickness of the active layers increases.[9] In addition, thin absorbing layers induce remarkable optical dissipation, which causes an inhomogeneous electromagnetic (i.e., optical) field distribution to form within the device that limits the harvested photocurrent (J_{SC}) despite internal quantum efficiencies (IQEs) approaching 100% for select architectures.[10]

To boost the light-harvesting efficiency of PSCs, researchers have developed sophisticated polymers with high carrier mobilities, which improves charge dissociation and transport in thick active layers (>180 nm).[11–16] Additionally, optical engineering was introduced to enhance light trapping in devices, and significant optical enhancement has been realized via a number of approaches in recent years. To capture the essence of these optical engineering strategies, we herein provide a comprehensive overview of recent developments in efficient PSCs with a focus on electrode engineering. First, we review the optical strategies exploited in PSCs thus far and follow with a detailed discussion on the diversity of electrode designs. The recently reported microcavity resonance effects arising from planar electrodes will be highlighted, due to the resulting enhancements in PSC photovoltaic performance. We conclude this review with a perspective on the future development of microcavity resonance effects for high-performance PSCs.

2. Optical Engineering in PSCs

To date, optical engineering has been applied extensively in PSCs to enhance the light absorption of the organic absorbers, which consequently improves their resultant EQEs. For a thin-film PSC in which the thickness of the active layer approaches the wavelength of the visible spectrum, the spatial distribution of the optical field within it is determined by the interference of incident light between the transmitted and reflected waves at each internal interface, which in turn affects charge generation within the organic absorbing layer.[17–19]

To date, a variety of strategies with distinct mechanisms has been employed to enhance the optical density in the photoactive region of PSCs. The most direct approach is to incorporate

Dr. C.-C. Chueh, M. Crump, and Prof. A. K.-Y. Jen
Department of Materials Science and Engineering
University of Washington
Seattle, WA 98195, USA
E-mail: ajen@u.washington.edu
Prof. A. K.-Y. Jen
Department of Chemistry
University of Washington
Seattle, WA 98195, USA

DOI: 10.1002/adfm.201503489

an additional anti-reflection (AR) layer (**Figure 1**a) or a light in-coupling texture at the front surface of device (Figure 1b). Such a buffer layer can reduce the reflection loss of the incident light and thus increase the light coupling into the device. For example, Xue et al. utilized a transparent polymeric microlens texture molded on the front side of the device to increase the light-trapping inside the organic active layer, resulting in a 15–60% enhancement in PCE (Figure 1d, left).[20] A polymeric retroreflective texture has also been successfully applied by Janssen et al. to alter the angle of the incident light and reduce the light reflection simultaneously, yielding a 19% increase in PCE (Figure 1d, middle).[21] More recently, Tang et al. integrated a moth eye antireflective texture along with the moth eye nanostructured active layer to yield a J_{SC} enhanced by 24.3% for the P3HT:$IC_{60}BA$ BHJ PSC and a promising PCE of 7.86% (Figure 1d, right).[22]

Incorporating an optical spacer in a stratified PSC is another facile way to increase the optical field inside the active layer. This additional layer can alter the optical interference inside a multi-layered device to modulate the intensity of optical filed in the photoactive region. Consequently, the exciton density generated in the active layer can be increased to improve the J_{SC} of the device.[23–28]

Constructing a multi-junction tandem PSC is another prevailing method used to improve light-harvesting efficiency.[2,29] The multi-junction configuration extends the optical path in the tandem PSC to maximize the total number of absorbed photons in the photoactive regions. In addition, the decreasing bandgap (E_g) of the individual sub-junctions broadens the light absorption window of the tandem PSC. Given these advantages, record-high PCEs of 11.3% and 11.8% in PSCs have been achieved in series-connected double-junction and triple-junction devices, respectively, where the sub-junctions with cascading E_gs were sequentially stacked.[5,30]

The decreased effectiveness of geometric light scattering for thin-film PSCs with active layer thicknesses comparable to the wavelength of the visible light[31–33] has inspired the recent development of coherent light-trapping strategies based on wave optics (Figure 1c).[17,18] By exploiting the wave nature of light, light trapping in the device can be enhanced through optical interference to confine the optical field of the incident radiations in the photoactive region. Based on this principle, numerous approaches including the use of photonic crystals,[34] metal nanomaterials and nanostructures,[35–39] and resonant cavities[40–43] have been employed to enhance the light-trapping and resulting PCE in thin-film PSCs.

To date, plasmonic-enhanced PSCs that employ metal nanomaterials or nanostructures in devices have attracted sizable research interest (Figure 1e).[35–37,39] The associated optical modes for plasmonic-enhanced PSCs mainly include quasi-guided modes (Figure 1e, left), surface plasmonic resonance (SPR) effects (Figure 1e, middle), and localized surface plasmon resonance (LSPR) effects (Figure 1e, right). In-depth, fundamental introductions of the underlying optical physics for plasmonic-enhanced PSCs can be found in other review articles.[17,18,35–37] Generally, employing nanostructured metal electrodes in the devices can induce SPR effects at the corresponding metal-organic interfaces. Meanwhile, LSPR effects can be introduced into the thin-film PSCs by incorporating metal nanomaterials into the constituent interlayers of the devices, such as the charge-transporting layers (CTLs) and the active layer. Notably, the LSPR peaks of the nanomaterials can be tailored by manipulating the size, composition, and shape of the nanomaterial.[43–54] We note that these plasmonic effects might have a more profound influence on organic absorbers than their inorganic counterparts due to their much smaller refractive indices, which can enable stronger overlapping between the derived plasmonic effects and the solar spectrum.

Chu-Chen Chueh received his Ph.D. in Chemical Engineering from the National Taiwan University 2010. In 2011, he joined Prof. Alex Jen's research group at the University of Washington. Currently, he is the leader of the organic–inorganic perovskite solar cells thrust in Prof. Jen's group. His research interests focus on organic/hybrid semiconductors and their applications in memory, light-emitting diodes, transistors, and solar cells.

Michael Crump received his B.S.E and M.S.E. (by thesis) in Materials Science and Engineering from the University of Pennsylvania in 2013 and 2014, respectively. Currently, he is pursuing his Ph.D. in Materials Science and Engineering at the University of Washington as a member of Prof. Alex Jen's research group. His research interests include photovoltaic device design and perovskite-based optoelectronics.

Alex Jen is the Boeing-Johnson Chair Professor and Chair of the Materials Science and Engineering Department at the University of Washington. He is also serving as the Chief Scientist for the Clean Energy Institute. For his pioneering contributions in organic photonics and electronics, he was selected as a Fellow by several professional societies such as AAAS, MRS, ACS, SPIE, OSA, and ACS-PMSE and a member of the Washington State Academy of Sciences. His research interests are in the area of organic functional materials and devices.

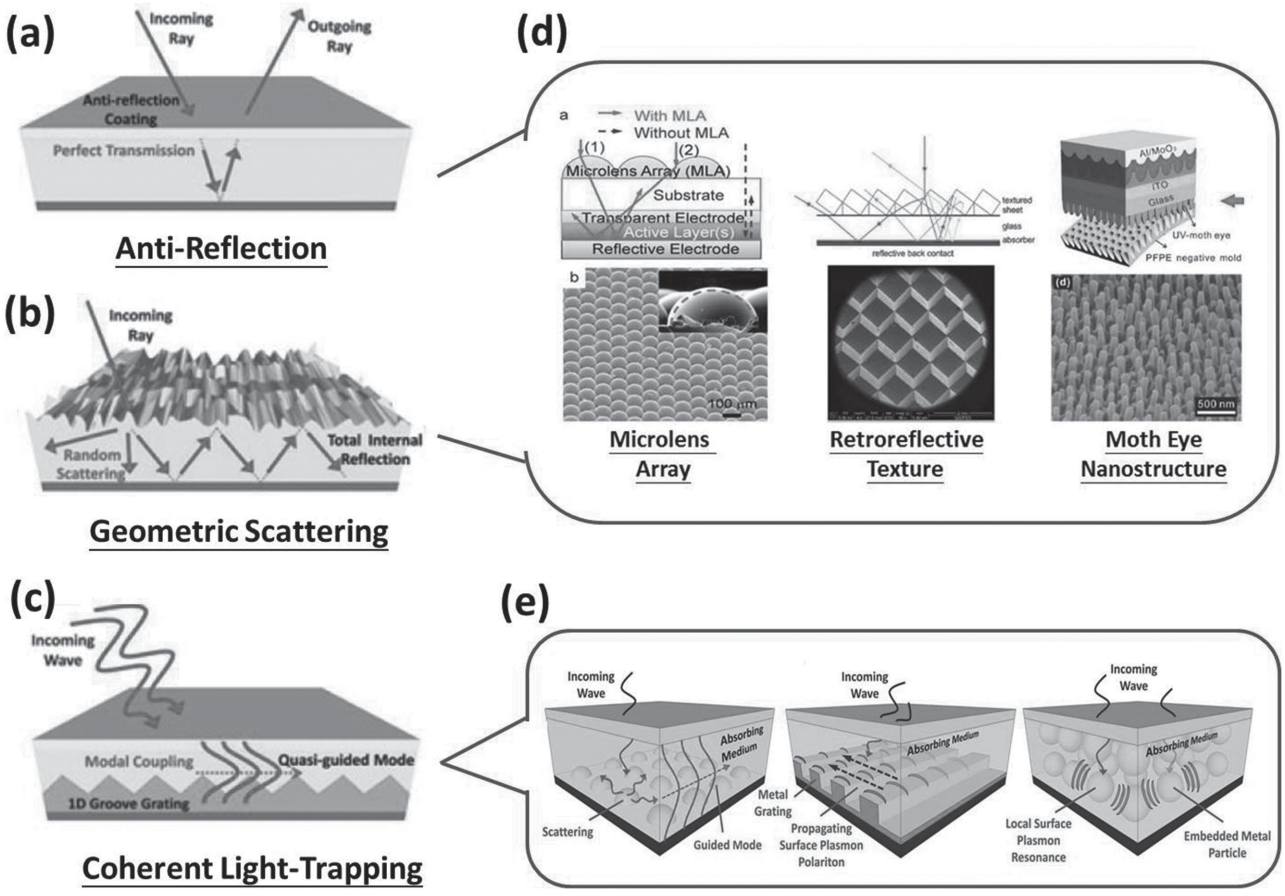

Figure 1. Illustration of the optical enhancement in the thin-film photovoltaics, including a) anti-reflection, b) geometric scattering, and c) coherent light-trapping, with d–e) its respective representative examples. a–c,e) Adapted with permission.[17] Copyright 2011, Cambridge University Press. d) (left) Adapted with permission.[20] Copyright 2012, The Royal Society of Chemistry. d) (middle) Adapted with permission.[21] d) (right) Adapted with permission.[22]

Recently reported plasmonic-enhanced PSCs utilize either LSPR, SPR, or a combination of the two to enhance light-trapping in devices. For instance, Hou and Choy et al. have introduced cooperative resonance effects of LSPR and SPR into the PSC by using dual plasmonic nanostructures in a device, where the gold nanoparticles (Au NPs) were embedded in the active layer along with a top silver (Ag) nanograting electrode.[52] As a result, the PCE of a PBDTTT-C-T:$PC_{71}BM$ BHJ device improved from 7.59% to 8.79%.

Lately, incorporating a microcavity structure in PSCs has also been proven as an effective approach to improve the light-trapping inside the device (**Figure 2**). Different from plasmonic-enhanced PSC, the microcavity-enhanced device is composed of planar electrodes that possess the reflectivity required to induce microcavity resonance inside the device. In principle, incident light with resonant frequencies will be optically confined and reinforced between two reflective electrodes due to coherent interference. To develop efficient microcavity-enhanced PSCs (MCPSCs), there are

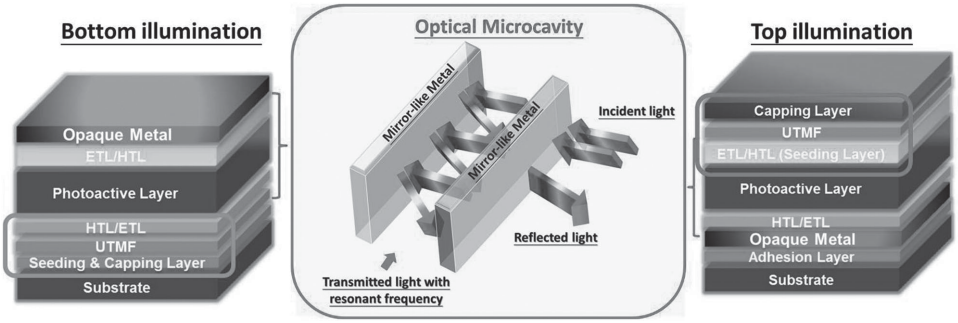

Figure 2. The typical device structures of microcavity-enhanced PSCs and illustration the of optical microcavity.

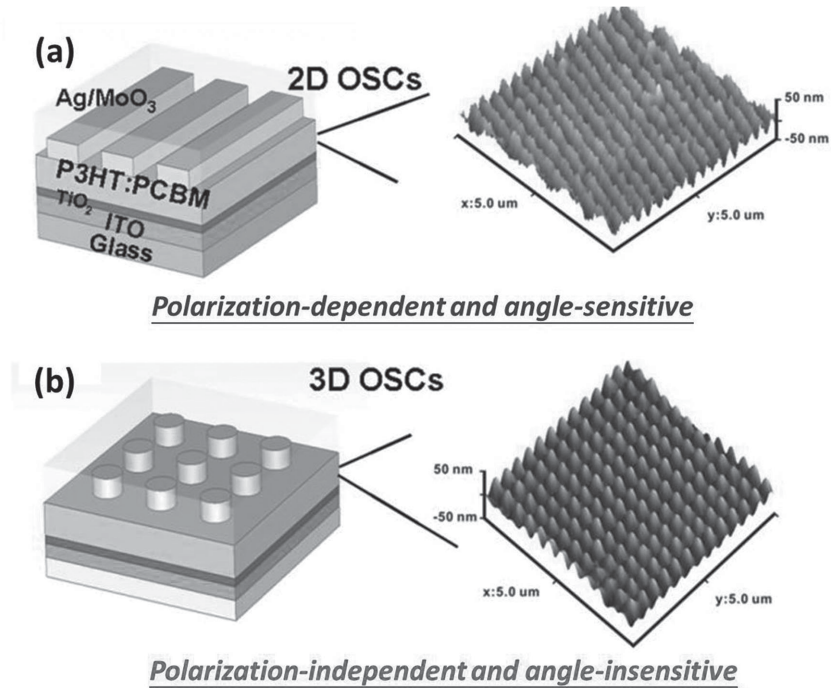

Figure 3. Comparison of a) 2D nanograting and b) 3D nanopatterned electrodes in thin-film PSCs. Adapted with permission.[38] Copyright 2014, The Royal Society of Chemistry.

several challenges that must be addressed, such as the growth of homogeneous ultra-thin metal films (UTMFs) and the reduction of refection loss caused by the reflective electrodes (Figure 2). In order to capture the essence of rapid developments of MCPSCs, we will focus on this microcavity resonance effect and its effects on MCPSC performance later in this review.

As discussed earlier, coherent interference between the transmitted and reflected waves inside the device determines the distribution of the internal optical field. Hence, the reflectivity and the parasitic absorption of the employed electrodes play an important role in the optical engineering of PSCs. Optimal electrodes should have minimized parasitic absorption and high internal reflectance throughout the visible spectrum to enable high optical density within PSCs.[26,28,55] Moreover, the recent achievement of plasmonic/microcavity-enhanced PSCs also displays the importance of electrode engineering to PSC performance enhancement.[56] Based on the distinct mechanisms used to induce optical coherence, we conclude that the electrodes employed in PSCs thus far can be divided mainly into two types: nanostructured and planar. In the following sections, we summarize the significant progress of electrode engineering employed in high-performance PSCs. We first review the recent progress of nanostructured electrodes for high-performance PSCs and then highlight recent developments of emerging MCPSCs derived from planar electrodes.

3. Nanostructured Electrodes in PSCs

Various designs of metal nanostructured electrodes have been exploited to improve the light-harvesting efficiency of PSCs thus far. They enhance light-trapping inside devices mainly through the geometric light scattering and plasmonic effects as described earlier. In principle, plasmonic effects can occur at the metal/organic interface when the incident light possesses a resonant frequency to the surface plasmon polariton (SPP) of the patterned electrodes. SPR effects can propagate along this corresponding interface, while LSPR effects are only confined in the proximity of specific nanostructrues.[17,18,35–37] Both effects are not only tightly bound to the associated interface with a skin depth of tens of nanometers, but also are strongly correlated with the geometry of the electrode. The electrode nanostructure will create distinct phase matching conditions between the incident light and SPP of the electrodes; thus the derived plasmonic resonance can be easily tuned from the visible to near-infrared (NIR) region via the rational design of the employed electrode.

3.1. 2D Nanostructured Electrodes

Among the variety of reported nanostructured electrode geometries, 2D metallic nanogratings were the primary structures utilized in PSC to improve light absorption by either serving as a semitransparent frontside electrode,[57,58] backside reflector,[43,59–62] or a combination of the two.[63] For example, Choy et al. successfully utilized Ag nanogratings as backside electrodes to improve the light-harvesting efficiency of several BHJ systems and the resultant PCEs. They prepared the nanostructured electrode by directly depositing the metal on a pre-imprinted active layer capped with an ultra-thin film (≈10 nm) of the hole-transporting layer (HTL) MoO_3 (**Figure 3**a).[62] Their experimental and theoretical results indicated that the observed optical enhancement stemmed from the synergistic effects of scattering and SPR induced by the 2D nanogratings. The enhanced absorption of high-energy photons arose from the waveguide modes, while the increase in low-energy photons resulted from the SPR effects. A high PCE of 7.73% with an increased J_{SC} (15.50 mA cm^{-2}) was achieved in the patterned PTB7:PC_{71}BM BHJ device, surpassing the PCE (7.20%) of the flat cell with a lower J_{SC} of 14.05 mA cm^{-2}. Furthermore, they integrated the plasmonic Au NPs embedded in the BHJ layer with this Ag nanograting backside electrode to enable a broadband absorption enhancement by collective resonance effects. Consequently, an impressive PCE of 8.79% with a high J_{SC} of 18.39 mA cm^{-2} was realized in the PBDTTT-C-T:PC_{71}BM BHJ device, which is much higher than the values (PCE: 7.59% and J_{SC}: 17.09 mA cm^{-2}) of the flat nanostructure-free device.[52]

However, the sensitive light polarization dependence of the 2D nanograting electrode causes the transverse electric (TE) and transverse magnetic (TM) modes to possess unequal light-trapping behavior in the derived device.[36,39,63] Choy and co-workers[64–66] revealed that only the TM wave, where the electrical field is perpendicular to the pattern direction of 2D nanograted electrode, could induce the SPR effects, while the

TE wave, where the electrical field is parallel to the pattern direction of electrode, contributed to other waveguide modes. Also, the derived SPR effects were largely dependent on the angle of incident light due to the intrinsic dispersive properties of the selected metal.[36] Such polarization- and angle-dependent optical properties of 2D nanograting electrodes are unfavorable for broadband optical enhancement. Therefore, 3D nanopatterned electrodes were investigated since they possess geometric symmetries associated with the different in-plane directions, enabling both TE and TM modes to excite SPPs in different directions at the organic/metal interface to reduce the polarization dependency.

Consequently, Choy et al. systematically compared the plasmonic response of 2D nanogratings with 3D nanocylinders (Figure 3b).[64] They demonstrated the benefits of the polarization-independent plasmonic response of the 3D patterned electrode, which yielded a higher PCE enhancement of 24.6% in the P3HT:PC_{61}BM BHJ device, surpassing the PCE enhancement of 17.5% obtained by the reference 2D electrode. Moreover, they also revealed that the increased interfacial area of the 3D patterned electrode improved charge collection at the corresponding metal/organic interface, reducing the series resistance (R_s) of the device.

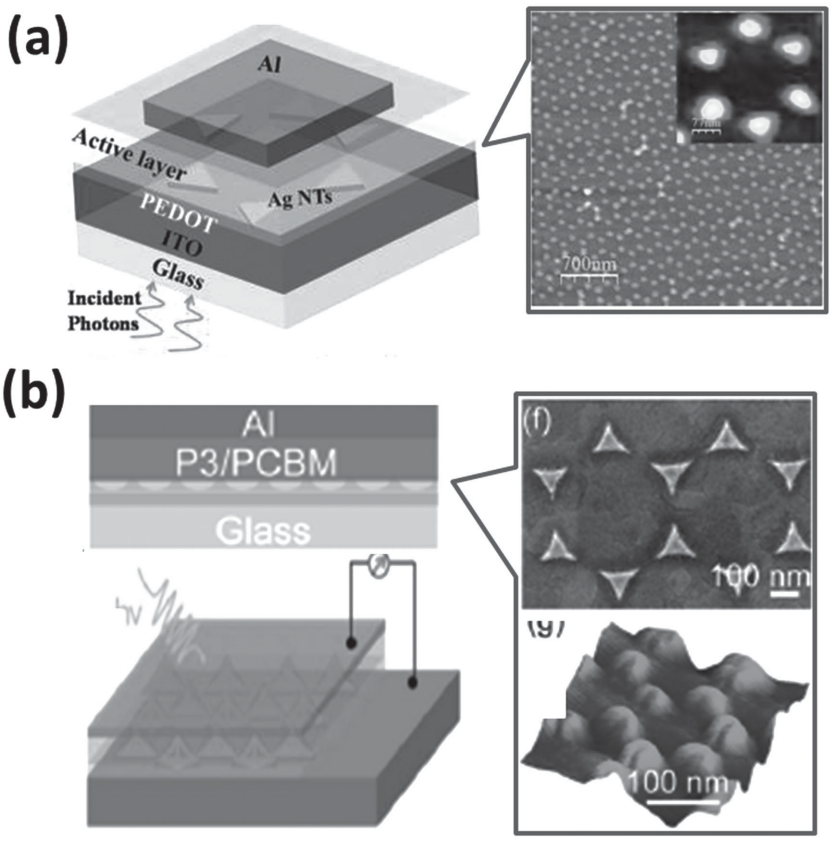

Figure 4. 3D a) nanotriangle- and b) nanopyramid-based electrodes used in thin-film PSCs. a) Adapted with permission.[68] Copyright 2012, American Chemical Society. b) Adapted with permission.[69] Copyright 2012, The Royal Society of Chemistry.

3.2. 3D Nanostructured Electrodes

The 3D patterned electrodes developed to date can be classified into two types: periodic metal arrays and randomly patterned metal nanostructures. For the periodic metal arrays, various nanostructures have been reported including hexagonal nanopillars,[67] nanotriangles,[68] nanopyramids,[69] and moth's eye nanostructures.[22,70] Similar to the 3D nanocylinders introduced earlier, Heeger et al. utilized a nanoimprinting method to fabricate a 3D-patterned IZO anode consisting of hexagonal-like nanopillars on a flexible substrate, which improved the PCE of a PCDTBT:PC_{71}BM BHJ device with a planar anode from 3.0% to 3.9%. This enhancement was attributed to the largely increased J_{SC} from 8.22 mA cm^{-2} to 10.26 mA cm^{-2} that resulted from improved light-trapping in the device.[67] Meanwhile, in separate reports Sum and Ren et al. decorated indium tin oxide (ITO) anodes with Ag nanotriangle and Au nanopyramid arrays fabricated by nanosphere lithography (NSL). They respectively yielded a ≈12% enhanced J_{SC} and a ≈31% enhanced PCE due to the scattering and LSPR effects introduced by these 3D electrodes, as illustrated in **Figure 4**.[68,69] Importantly, the sharp edges of the nanotriangles/nanopyramids induced more intense LSPR effects than spherical NPs, thus increasing absorption.

Most recently, Li and Tang et al. have reported a quasi-periodically biomimetic moth eye nanostructure prepared by soft nanoimprinting lithography (Figure 1d, right).[22] Not only used as a frontside antireflective texture as discussed, this nanostructure was also simultaneously employed as a backside electrode to enable large, polarization-independent enhancement in broadband absorption, which results from the reduced reflectance and induced SPR effects. As a result, an enhanced PCE from 6.43% to 7.86% was realized in a P3HT:IC_{60}BA BHJ PSC with these nanostructured electrodes because J_{SC} increased from 12.20 mA cm^{-2} to 15.16 mA cm^{-2}. In addition, they incorporated this nanostructured electrode architecture into a PTB7:PC_{71}BM BHJ system to achieve a promising PCE of 9.33% with a ≈20% enhanced J_{SC} compared to the control device, demonstrating the great efficacy of this device architecture.[68]

The development of randomly patterned metal electrodes for high-performance PSCs also has progressed in recent years.[71–73] One representative example is a random array of aperture electrodes.[46,74–76] Hatton et al. first reported an ultrathin Au electrode with microscale large-size apertures by applying microsphere lithography to an ultrathin Au film evaporated on to various molecular adhesives (**Figure 5**a).[75] However, these large-size apertures in the electrode induced only detrimental geometric scattering effects, not plasmonic effects. Such scattering induced by the microscale apertures resulted

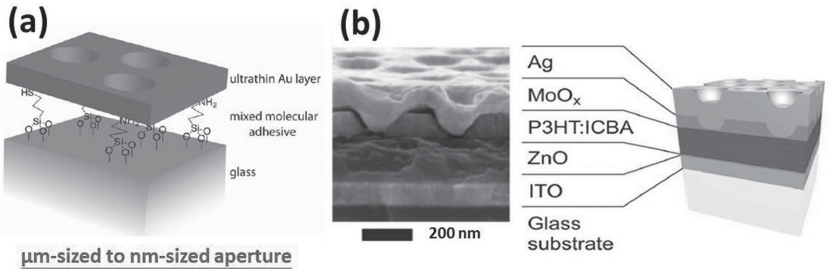

Figure 5. 3D a) aperture, where the microscale one is plasmonic-inactive while the nanoscale one is plasmonic-active, and b) nanoknob electrode used in thin-film PSCs. a) Adapted with permission.[75] b) Adapted with permission.[78]

in inferior far-field transmittance compared to that of the pristine ITO electrode, leading to a ≈10% loss in the resultant J_{SC}. So, they next fabricated an electrode with a high density of nanoscale small-size apertures via a lithography-free approach. The processing conditions of the molecular adhesives were carefully controlled to reduce the surface coverage of the adhesives, which promoted the formation of dense nanoscale apertures in the evaporated metal film.[76] These electrodes with sub-wavelength apertures not only demonstrated strong coupling with incident light but also excited SPPs near the perimeter of the aperture, thus increasing the optical density near the metal/organic interface to enhance light-trapping in the device. Consequently, these nano-sized aperture electrodes yielded enhanced J_{SC}s for PCDTBT:PC_{71}BM BHJ devices on both glass and plastic substrates. A flexible PSC with an improved PCE from 4.6% to 5.1% was demonstrated, validating the superior mechanical and plasmon-active advantages of this nano-sized aperture electrode.

Additionally, nanoscale indented electrodes were developed to enhance the photovoltaic performance of PSCs.[77,78] Rand et al. utilized non-destructive hole-mask colloidal lithography (HCL) to fabricate a plasmon-active indented backside electrode to enhance the PCE of a P3HT:IC_{60}BA BHJ PSC by ≈5% (Figure 5b).[78] Notably, they observed that the indent feature size could be tuned such that the LSPR coincided with the absorption edge of the organic absorber to maximize optical enhancement.

Recently, Huang et al. utilized a Blu-ray disc (BD) as a nanoimprinting template to fabricate a quasi-random nanostructured electrode to enhance PSC performance (**Figure 6**a).[79] Their analysis of the Fourier transforms of the subwavelength features suggested that the light-trapping capability of the BD pattern was comparable to that of quasi-random pattern due to its effective light coupling into the waveguide and SPR modes.[79,80] As a result, a PTB7:PC_{71}BM BHJ device using a BD patterned electrode delivered a 16.9% enhanced J_{SC} and a 11.9% increased PCE compared to the flat control device. Most recently, Oh and Hwang et al. employed an Ag nanowire (NW) mesh electrode to fabricate a highly efficient flexible PTB7:PC_{71}BM PSC (Figure 6b).[81] They revealed that the optical enhancement introduced by this mesh electrode resulted from both geometric scattering and SPR effects as supported by their finite difference time domain (FDTD) simulation, which defined a prominently enhanced optical filed around the Ag

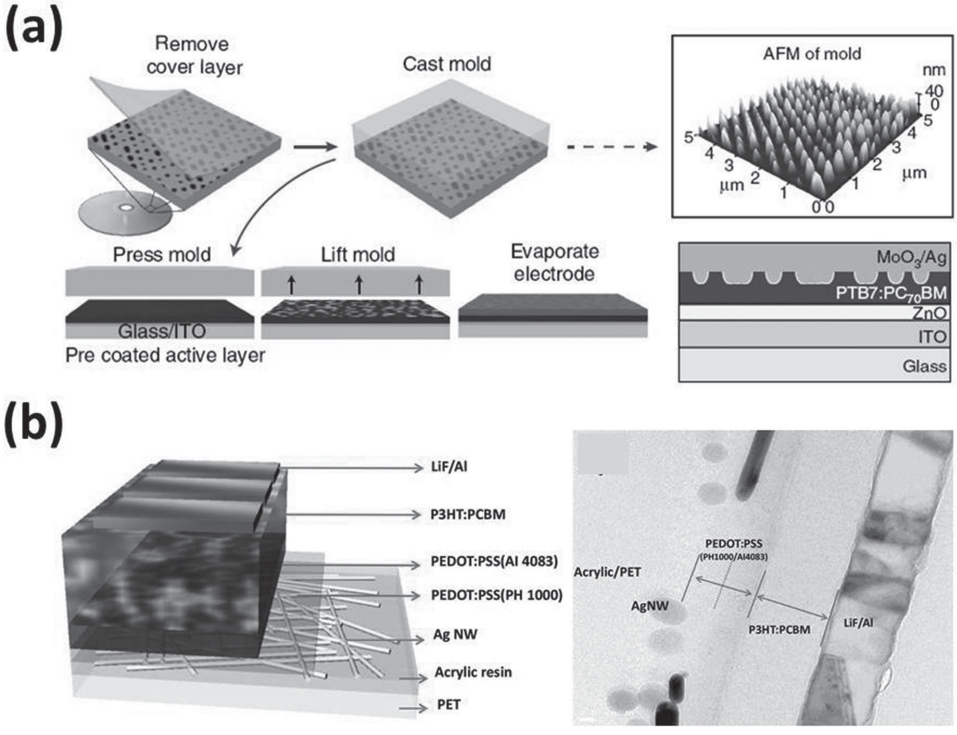

Figure 6. a) Blu-ray disc (BD) patterned electrode and b) Ag nanowire (NW) mesh electrode employed in thin-film PSCs. a) Reproduced with permission.[79] Copyright 2014, Nature Publishing Group. b) Reproduced with permission.[81]

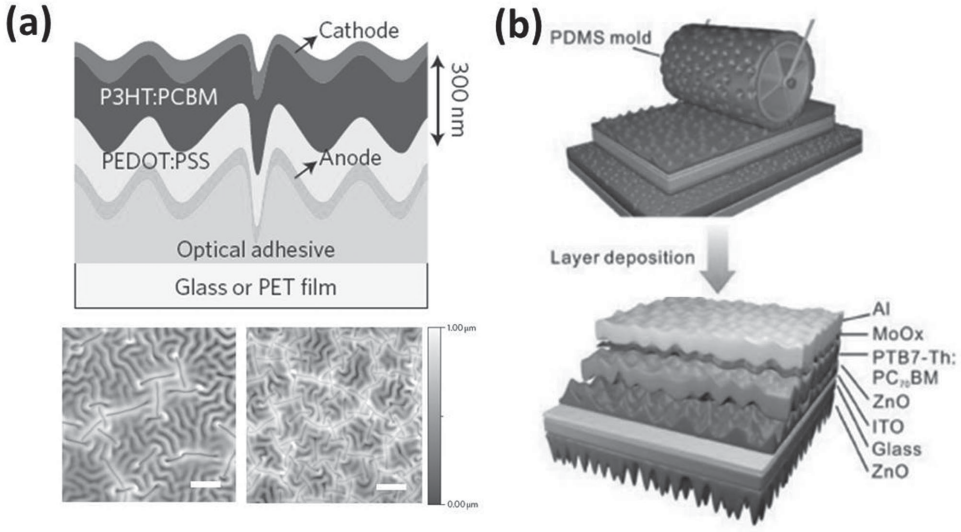

Figure 7. Thin-film PSCs with the device configuration of a) wrinkled nanostructure associated with deep folds and b) deterministic aperiodic nanostructures (DANs). a) Reproduced with permission.[33] Copyright 2012, Nature Publishing Group. b) Reproduced with permission.[82]

NWs. Finally, a highly efficient flexible PTB7:$PC_{71}BM$ BHJ device with a decent bending durability was demonstrated (PCE: 7.58%), which surpassed the performance of the control device using a rigid ITO/glass substrate (PCE: 7.12%).

Randomly wrinkled architectures with deep folds also were exploited by Loo et al. to enhance the light-trapping in PSCs recently.[33] As displayed in **Figure 7**a, excessive compressive stress was applied to an optical adhesive on a glass substrate to create a template of wrinkles and deep folds for the evaporated Au anode. They revealed that the geometric refraction arising from both the wrinkles and deep folds in the anode introduced strong waveguiding properties to trap the light inside the device efficiently; however, the strongest enhancements in light trapping fell in the NIR region and were non-linear across the solar spectrum. Accordingly, a device using this wrinkled template with deep folds improved EQE in the NIR region (>650 nm) over 600%, resulting in a 47% enhanced J_{SC} compared to that of the pristine planar device. Encouragingly, these wrinkled structures could relieve mechanical stress, enabling the exceptional bending durability observed for these device.

Based on their previous report describing the incorporation of moth eye nanostructured electrodes in thin film PSCs, Tang and Li et al. further developed wrinkle-like deterministic aperiodic nanostructures (DANs) to enhance broadband optical absorption by PSCs with minimized charge recombination.[82] DANs were first patterned onto the substrate by a facile rolling nanoimprinting technique, which was followed by sequential layer deposition to complete device fabrication (Figure 7b). By applying this nanoimprinting onto both sides of ITO/glass, a completed DAN-based device with both patterned anti-reflective texture and backside electrode was fabricated with an architecture similar to that used in the moth eye nanostructured device (Figure 1d, right). Benefitting from the collective effects of reduced reflection, enhanced light scattering, and SPR, the fabricated DAN-based PTB7-Th:$PC_{71}BM$ BHJ device delivered an impressive PCE of over 10%, representing 18% and 20% enhancements in J_{SC} and PCE, respectively.

4. Planar Electrodes: Optical Microcavity

4.1. Microcavity Resonance

Adopting a metallic reflective microcavity configuration in thin-film PSC recently emerged as an effective approach to enhance the light-trapping inside the device. This resonant cavity design has been used commonly to enhance the performance of photodetectors and light-emitting diodes (LEDs) previously.[83–85] An optical microcavity is formed when a thin organic absorbing layer is sandwiched by two reflective electrodes. Ideally, these reflective electrodes are located at the nodes of the optical field to achieve constructive interference within the device. The conditions for constructive interference also can be met if the optical length of the chamber equals a multiple integer of the wavelength of the incident light. In addition, the phase change of the field induced by reflection at each electrode must be taken into account when determining the optical path length of the incident light. Consequently, the optically resonant condition for the light with a certain wavelength (λ) can be formulated by Equation (1),[43,86]

$$\sum_i \eta_i d_i + (\psi_1 + \psi_2)\frac{\lambda}{4\pi} = \frac{m\lambda}{2} \quad (1)$$

where η_i is the real part of the refractive index, d_i is the thickness of the film between two electrodes, ψ_1 and ψ_1 are the respective phase changes due to the reflection at the each interface, and m is a positive integer.

Once this constructive interference condition is satisfied, incident light with resonant frequencies can be trapped effectively in this optical microcavity.[43,86–89] Therefore, the microcavity resonance can improve the light-trapping inside the devices only over a narrow spectral and angular range. Therefore, the optical field distribution and the resonance effects inside the devices need to be carefully controlled to suppress optical dissipation arising from the non-resonant wavelengths.

More importantly, a PSC with an active layer thickness comparable or smaller than the wavelength of visible light will exhibit much stronger resonance induced by a microcavity structure because coherent interference within the film weakens as film thickness increases.[83–86]

To develop efficient MCPSCs, two important factors need to be addressed: the constituent interlayers inside the resonant cavity and the choice of electrodes. Most high-performance PSCs reported to date incorporate CTLs with organic absorbers to achieve efficient charge dissociation and extraction. Such a multilayered architecture will affect the resonant conditions of the microcavity chamber because these CTLs will alter the reflection at the BHJ/electrode interfaces, resulting in asymmetric optical field distributions. Long has suggested that the thickness of the CTLs greatly influenced the total absorbed photons (TAPs) of the central active layer in the microcavity structure by optical simulation based on the transfer-matrix method (TMM).[87] Additionally, he further showed that these CTLs can serve as optical spacers to significantly enhance the TAPs of the thin BHJ layer (<80 nm, P3HT:$PC_{61}BM$). Consequently, a 70 nm thick BHJ layer in the optimized microcavity device possessed a TAPs equivalent to that of a non-cavity device with a 200 nm-thick active layer, representing a 16.3% optical enhancement as compared to the non-cavity device using the same BHJ thickness. Subsequent demonstrations of employing CTLs as optical spacers in microcavity structures were reported by several groups;[88,90,91] as exemplified in **Figure 8**, the optical field distribution of the formed resonant cavity were influenced by the employed CTLs in the devices.[91]

The proper choice of a transparent electrode is another important factor when designing an effective microcavity structure. Transition metal oxides (TMOs), such as ITO and fluorine-doped tin oxide (FTO), are the most commonly used electrodes because they feature both high transparency (≈82% in the visible spectrum) and conductivity (low resistivity of 10–20 Ω $\square^{-1}$).[92] While ITO can be used in a microcavity configuration in a PSC, its high transparency limits its potential as a resonant cavity because a large fraction of unabsorbed photons will escape from the device. To address this issue, Long inserted a thin TiO_2 layer at the ITO/glass interface to serve as a dielectric mirror that increased the microcavity resonance effects in the regular ITO-based PSCs.[88] However, the high transparency of TiO_2 still made the bi-layered electrode suffer from large optical dissipation, limiting the efficacy of the device.

In this regard, reflective and transparent ultra-thin (<10 nm) metal films (UTMFs) have been employed widely as a mirror-like planar electrode to achieve high-performance MCPSCs due to their compatibility with organic semiconductors and simple processability by thermal evaporation. The superior reflective transparent properties of UTMFs compared to ITO ensure a stronger microcavity is formed to yield more effective optical confinement inside the active layer. Furthermore, these UTMFs can possess a higher conductivity than ITO and thus become a promising candidate for developing ITO-free PSCs.[93] It is well known that ITO has several inherent disadvantages, such as a delicate depositing process, poor ductility and high sheet resistance (R_{sheet}) (≈60 Ω $^{-1}$) on flexible substrates, and the scarcity of indium.[93] Hence, a UTMF-derived microcavity configuration not only can provide improved light-trapping for thin-film PSCs but also can result in stable, efficient, ITO-free, and flexible device architectures. In the following sections, we review recent developments of UTMFs in MCPSCs and the resulting enhancements in photovoltaic performance.

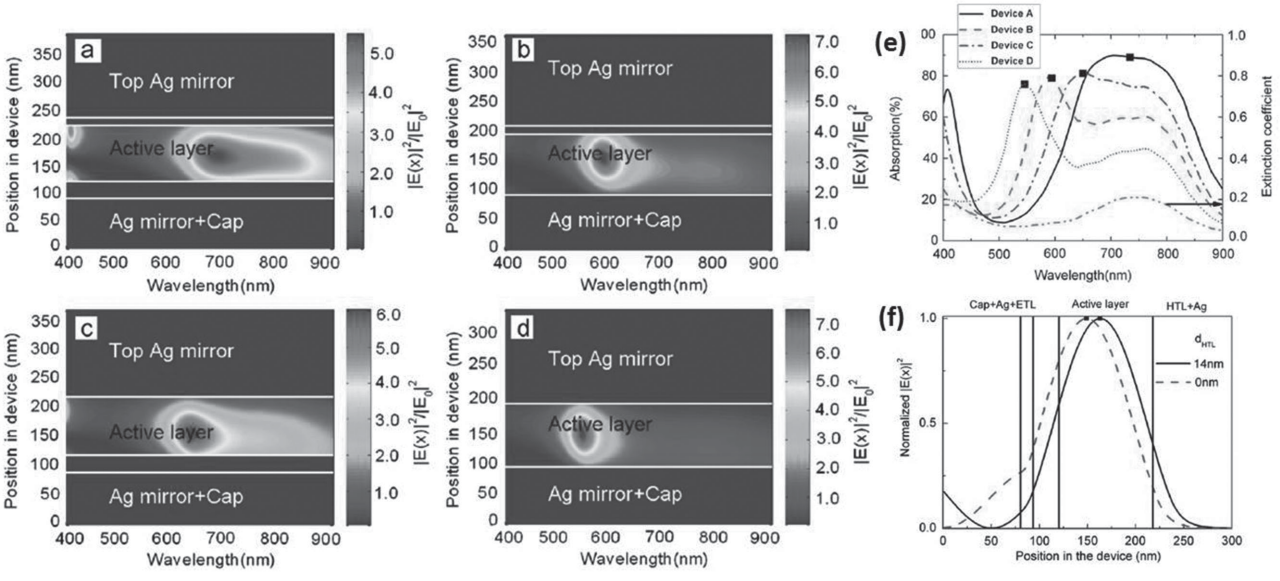

Figure 8. a–d) Distribution of the optical electric field $|E(x)|^2$ in MCPSCs with or without using the CTLs, where the ETL is ZnO with a thickness of 30 nm while the HTL is MoO_3 with a thickness of 14 nm. a) ITO/thin Ag/ETL/BHJ/HTL/Ag (Device A); b) ITO/thin Ag/BHJ/HTL (Device B); c) ITO/thin Ag/ZnO/BHJ/Ag (Device C); and d) ITO/BHJ/Ag (Device D). e) The absorption spectra of the devices shown in (a–d). f) Normalized $|E(x)|^2$ of a 734 nm light wave (incident from the left) in Device A with different HTL thickness. All the optical electric filed shown here is calculated by the optical modeling based on TMM. Reproduced with permission.[91] Copyright 2011, Elsevier.

4.2. Ultra-Thin Metal Film (UTMF)

To obtain an effective, mirror-like UTMF, the uniformity, thickness, and reflective transparent properties of the film must be controlled carefully. As shown in Figure 2, both seeding and capping layers commonly are required to fabricate an effective UTMF electrode used in a microcavity structure. In a conventional bottom-illuminated configuration, an interfacial film can function simultaneously as the seeding and capping layer, while this film can serve as a capping layer and a CTL in the top-illuminated structure (a separate capping layer is required for the latter). In the next two subsections, we define and elucidate the importance of these interfacial layers in MCPSCs.

4.2.1. Uniform Thin-Film Growth of UTMF

In addition to applications in MCPSCs, effective UTMF-based electrodes are also very important for the development of semi-transparent PSCs.[94,95] Among all UTMFs explored to date, Ag is the most commonly used metal because it has the lowest resistivity (1.62 μΩ cm), highest optical transparency, and remarkable flexibility that is inferior only to Au.[43] Nevertheless, the physical properties of any UTMF will be greatly influenced by the quality of the thin film rather than the bulk materials properties of the metal. In principle, the quality of a UTMF is determined by its nucleation and growth kinetics. Taking Ag UTMFs as an example, several distinct growth modes have been investigated, including the Volmer-Weber mode ("island" mode) and the Stranski-Krastanov mode ("layer-plus-island" mode),[96–98] indicating that the surface energy (γ) of the substrate and the vacuum deposition rate will affect the physical properties of UTMFs.

The conductivity and optical properties of Ag UTMFs deteriorates when film thickness dips below its percolation threshold (empirically measured to be ≈10 nm) as a result of the inhomogeneous, island-like film formation associated with the Volmer-Weber growth mode. This rough, discontinuous surface leads to undesired optical scattering and decreased conductivity. The compatibility between the Ag UTMF and the underlying substrate determines the percolation threshold; therefore, high compatibility between these layers is desired to minimize film thickness and to ensure uniform film morphology.[28,44,99]

It has been recognized that the tradeoff between the resistance and transparency of UTMF strictly depends on its thickness. A thick UTMF might incur unsatisfactory transparency, while an excessively thin UTMF could result in a high R_S. Therefore, a proper seeding layer is necessary to facilitate the uniform thin-film growth of UTMF to be as thin as possible (≈ 10 nm) to maintain high conductivity and transparency.[28,44] The purpose of this seeding layer is to modulate the surface energy (γ) of the substrate to improve the compatiblity between molten Ag and the substrate. Note that the seeding layer itself also must be highly transparent to avoid any parasitic absorption losses.

Various kinds of seeding layers for UTMFs have been investigated so far, such as thin metals,[100–103] TMOs,[104–107] and organic materials.[41,108–110] Recently, Schuberts et al. systematically studied Ag UTMFs grown on various ultra-thin metallic seeding layers, including calcium (Ca), aluminum (Al), and Au to investigate surface wetting issues during thin-film growth.[103] As shown in **Figure 9**a, the surface morphology of Ag UTMFs on MoO_3 is rough, but the morphology improves as the surface energy of the seeding layer increases. The Au seeding layer delivers the smoothest surface, resulting in the highest conductivity and transmittance of the resultant Ag UTMFs (Figure 9b). A 7 nm Ag UTMF grown on 1 nm Au had an R_S of ≈19 Ω^{-1} and a high transmittance of 83% at 580 nm, which are comparable to the values of a conventional ITO electrode. They utilized this composite UTMF electrode to fabricate an MCPSC (PCE: 4.7%) that slightly exceeds the PCE of the pristine UTMF-free device (4.6%).

Utilizing TMOs as seeding layers in a dielectric/metal/dielectric (D/M/D) electrode is another widely used method[110,111] because they possess excellent γ compatibility with molten Ag, which facilitates homogeneous thin-film growth. In addition, the large dielectric constant (ε) of these TMOs enables them to serve as an effective capping layer to enhance the optical transmittance of the adjacent UTMFs. A more detailed discussion pertaining to capping layers incorporated with UTMFs will be discussed in the next subsection. Besides studying various metallic seeding layers, Schubert et al. also have investigated Ag UTMF formation on different TMOs, including molybdenum trioxide (MoO_3), tungsten oxide (WO_3), and vanadium oxide (V_2O_5).[106] Figure 9c shows the improved surface morphology of all UTMFs after introducing the TMO-based seeding layers, especially for MoO_3. This enhancement in UTMF formation thus results in improved transmittance in the red/near-IR regime (>600 nm) (Figure 9d), the most efficient absorption region of the studied organic absorber. Encouragingly, these TMO-supported MCPSCs not only delivered improved PCEs but also showed superior ambient stability and flexibility compared to the control ITO device. In addition, the TMO-based seeding layers in the top-illuminated configuration also functioned as CTLs (Figure 2). For example, for the devices used in Figure 9c–d, the TMO-based seeding layers simultaneously served as HTLs. Therefore, the corresponding charge-transporting capability of the TMOs also needs to be taken into consideration while designing high-performance, TMO-supported MCPSCs.

Organic-based D/M/D electrodes have also attracted much attention in recent years. Several groups have demonstrated that the organic CTLs can serve as effective seeding layers in the top-illuminated MCPSCs. For instance, Lee et al. have utilized bathocuproine (BCP) to fabricate a BCP/Ag/MoO_3 electrode, where the BCP simultaneously serves as a ETL and a hole-blocking layer in the device.[108] Recently, Jen et al. employed a fullerene-based (Bis-C_{60}) seeding layer to build a Bis-C_{60}/Ag/tellurium dioxide (TeO_2) electrode that yielded highly efficient, flexible MCPSCs with remarkable bending durability; in addition, Bis-C_{60} was used serve as an efficient optical spacer and conductive ETL in the device.[28,112,113] More detailed applications of these UTMFs in high-performance MCPSCs will be introduced in Section 4.3.

4.2.2. Capping Layers for UTMF

As illustrated in Figure 2, there exists a compromise between the transmittance and reflectance of the incoming light incident

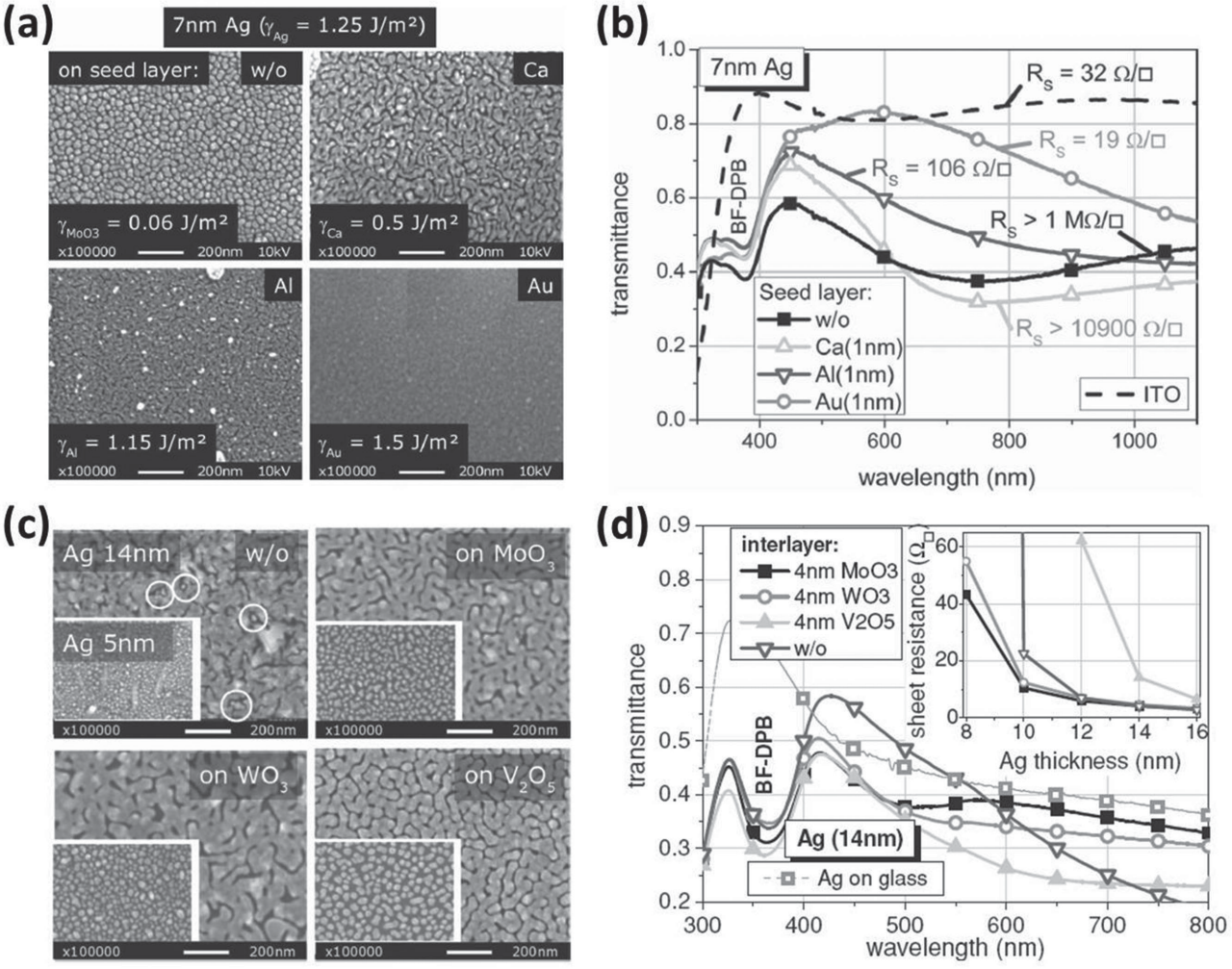

Figure 9. SEM images of a) 7 nm Ag UTMF deposited on top of different metallic seeding layers with distinct surface energy (γ) and c) 5 and 14 nm Ag deposited on different TMOs. b,d) The transmittance and R_S of the Ag UTMFs shown in (a) and (c). a,b) Reproduced with permission.[103] c,d) Reproduced with permission.[106]

to a UTMF. In order to minimize the reflected fraction of the incident light, a capping layer that behaves like an anti-reflective coating must be indirect contact with the UTMF. Note that the dielectric constant (ε) of this layer greatly influences the resulting optical properties of the adjacent UTMF. As illustrated in **Figure 10**a,[104] an Ag UTMF grown on a capping layer (also serving as a seeding layer herein) with a small ε (<9.7) will suffer a large optical dissipation due to the emission of non-radiative surface plasmons (SPs) at the dielectric-Ag interface, and thereby reducing its optical transparency. However, such SP

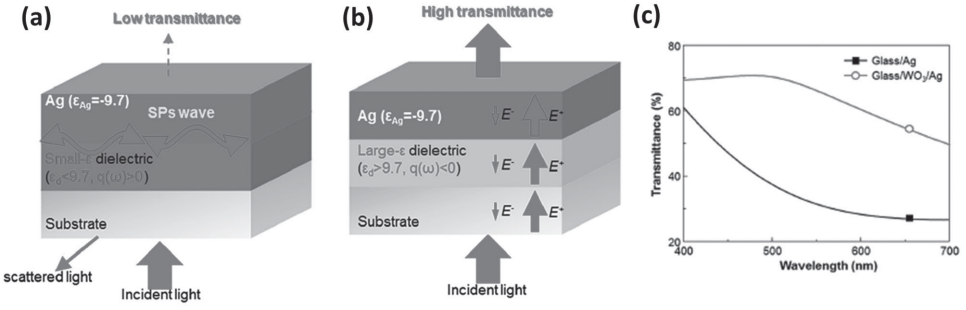

Figure 10. Illustration of the transparency mechanism of a D/M/D electrode with a) a small-ε dielectric/Ag (10 nm) and b) a large-ε dielectric/Ag (10 nm). c) Transmittance spectra of glass/Ag (10 nm) and glass/WO_3 (30 nm)/Ag (10 nm). Reproduced with permission.[110] Copyright 2012, Society of Photo Optical Instrumentation Engineers.

coupling can be effectively suppressed by using capping layers with high ε (>9.7), which consequently increases the optical transparency of the adjacent UTMF (Figure 10b). Therefore, TMOs with large ε have been extensively employed as the capping layers in the D/M/D electrodes. Figure 10c demonstrates that an Ag UTMF (10 nm) deposited on WO_3 ($\varepsilon = 35.2$), serving as both capping layer and seeding layer in this example, exhibited improved transmittance across the visible region, surpassing that of the Ag UTMF grown on glass ($\varepsilon = 5.7$).[105]

This discussion underscores the importance of interfacial layers when fabricating a high-quality UTMF, which is a prerequisite for an efficient MCPSC. With this in mind, we summarize the recent progress of high-performance MCPSCs with UTMFs.

4.3. Microcavity-Embedded PSCs

4.3.1. Single-Junction PSCs

Based on the previous achievements by Long and Kim et al.,[86–88,90,91] MCPSCs have achieved rapid progress in recent years. Various composite UTMFs as discussed previously have been used to fabricate effective microcavity configurations to enhance the light-trapping within PSCs. For metallic bi-layered UTMFs, Ghosh et al. reported a MCPSC derived from a Cu-Ni UTMF electrode.[114] Owing to the low percolation threshold of Cu (5.5–6.5 nm), they did not incorporate a seeding layer. Therefore, the electrical properties of this bi-layered electrode were directly determined by the quality of the Cu UTMF. As shown in **Figure 11**b, the conductivity of this bi-layered UTMF dramatically increased when the Cu UTMF exceeded 7 nm. The thin Ni layer served as a work function (WF) modifier (Figure 11a) to shift the WF of pristine Cu from 4.65 eV to 5.06 eV (Cu–Ni), enabling better hole extraction, and to enhance the stability of Cu (Figure 11b, insert). As a result, the MCPSC derived from the optimized Cu–Ni electrode yielded a performance comparable to the value of the ITO device due to the microcavity resonance effects, despite the fact that Cu–Ni UTMF possessed only 65% of the transparency of ITO (Figure 11c-d).

As discussed earlier, TMO-based D/M/D electrodes are the most widely used UTMFs for MCPSCs to date. Shen and Long et al. first investigated the efficacy of WO_3–Au–WO_3 UTMF-based MCPSCs in various BHJ systems.[115–118] They reported that the strength of the microcavity resonance was strongly correlated with the thickness of the active layers used in the devices. As shown in **Figure 12**a, the microcavity-enhanced J_{SC} was observed in the thin PCDTBT:$PC_{71}BM$ (70 nm) device, boosting the PCE from 4.28% to 4.55%.[116] However, the J_{SC} of the microcavity device decreased when using a thicker BHJ layer (130 nm), resulting in inferior performance relative to the ITO control device. The TMM optical simulation results shown in Figure 12b suggested that the optical resonant cavity contributed to a stronger optical field in the thin BHJ device

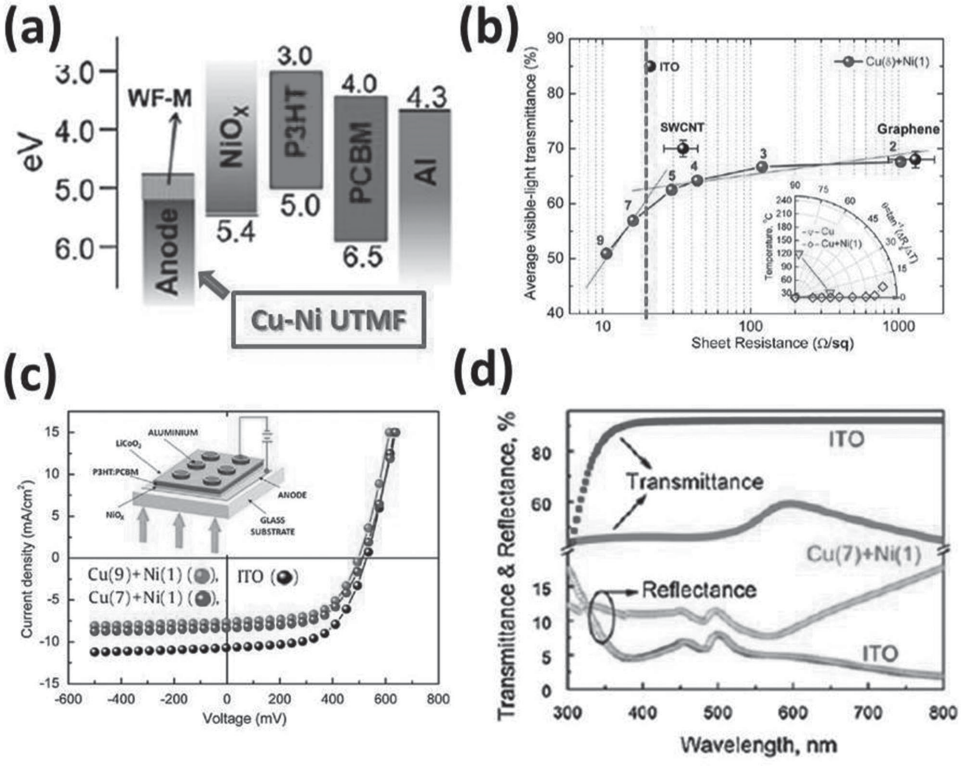

Figure 11. a) Energy level diagram of MCPSC based on Cu-Ni UTMF, where Ni acts as a WF modifier of Cu. b) Comparison of optical transmittance of Cu-Ni UTMFs with other common transparent electrodes (ITO, graphene, and single walled carbon nanotubes (SWNT)); insert is the polar Figure for thermal stability of the Cu-Ni UTMFs compared with the pristine Cu UMTF in terms of R_S change. c) *J–V* curves of MCPSCs (insert) using different electrodes. d) Comparison of transmittance and reflectance of Cu (7 nm)–Ni (1 nm) UTMF with ITO. Adapted with permission.[114] Copyright 2011, Elsevier.

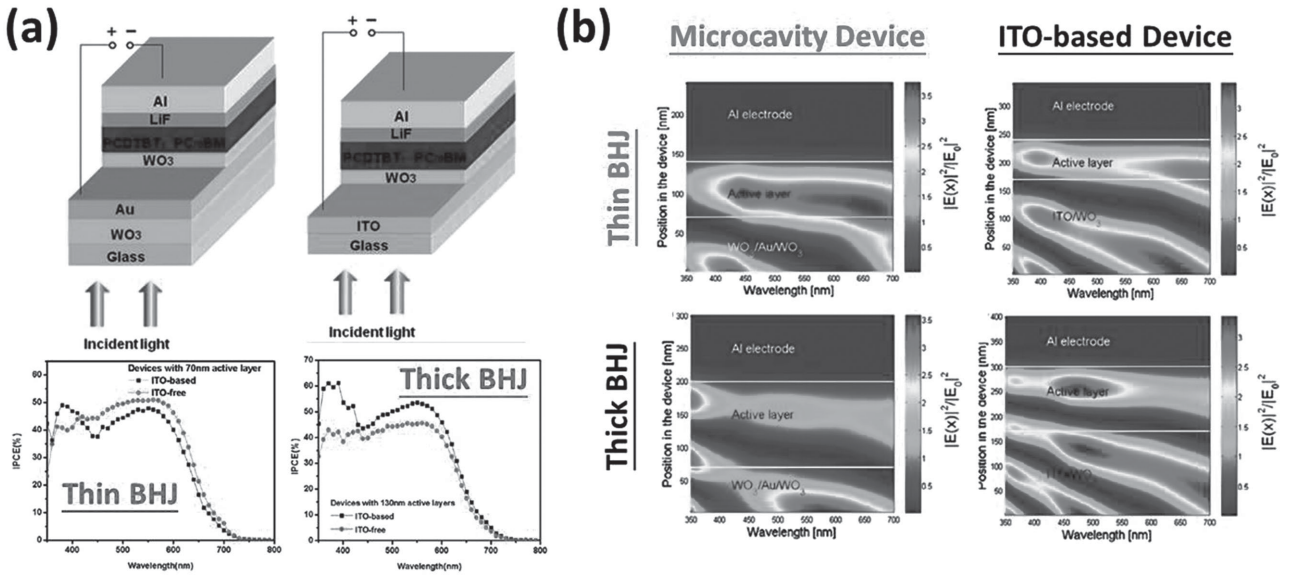

Figure 12. a) (top) Device architectures of the WO_3/Au/WO_3 based MCPSCs and the control ITO-based PSCs. (bottom) The corresponding EQE curves of these devices with thin and thick BHJ layers. b) Distribution of the optical electric field $|E(x)|^2$ in the devices with thin and thick BHJ layers as simulated by TMM optical modeling. Adapted with permission.[116] Copyright 2014, Elsevier.

compared to the regular ITO device, while this enhancement diminished as the BHJ thickness increased. Once the resonant cavity effects were weakened, detrimental off-resonance effects emerged, reducing the light absorption and resultant J_{SC} of the device.

Based on the same BHJ system, Rand et al. subsequently fabricated an MoO_3–Ag–MoO_3 UTMF-based MCPSC as shown in **Figure 13**a.[41] They revealed the Ag UTMF (6 nm) deposited on a thin MoO_3 (2 nm) seeding layer possessed a much lower R_S (6.2 Ω □$^{-1}$) than ITO (18 Ω □$^{-1}$). They also illustrated that the resonant cavity width could be modulated by tuning the HTL thickness since it served as an optical spacer that could affect the resonant condition of the resulting microcavity in the device. Therefore, microcavity resonance effects could be manipulated to compensate for weak absorption at any given wavelength. As a result, the optimized thin-film PCDTBT:$PC_{71}BM$ (55 nm) MCPSC delivered a PCE of 4.44%, comparable to the value of the control ITO device (PCE of 4.43%). Meanwhile, Meredith et al. independently employed similar MoO_3–Ag–MoO_3 UTMF electrodes to fabricate a top-illuminated large-area sub-module

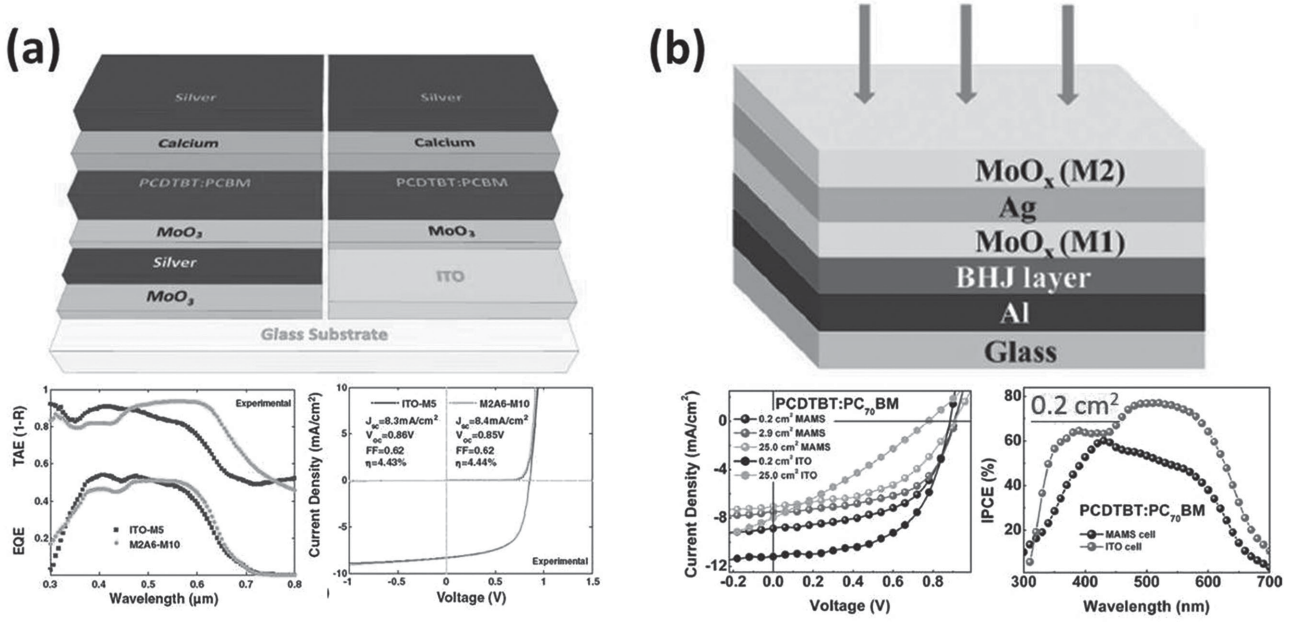

Figure 13. MoO_3–Ag–MoO_3 UTMF-based MCPSCs: a) bottom-illuminated and b) top-illuminated configurations. Adapted with permission.[41] Adapted with permission.[119]

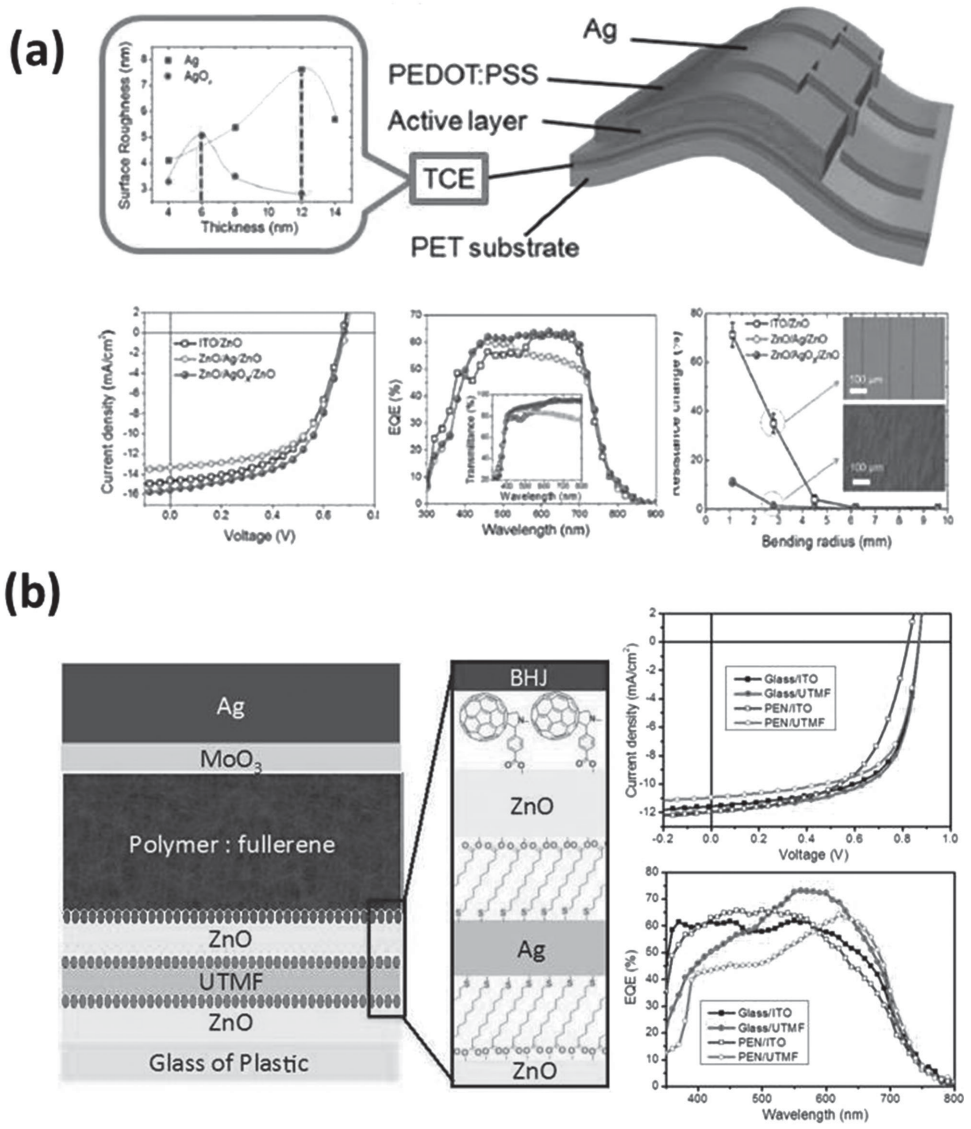

Figure 14. a) ZnO–Ag(O_X)–ZnO UTMF based flexible MCPSCs and b) SAM-modified ZnO–Ag–ZnO UTMF based MCPSC. a) Adapted with permission.[120] b) Adapted with permission.[121]

of MCPSC (Figure 13b).[119] Benefitting from low R_S (5.0 Ω □$^{-1}$) and coherent optical interference effects introduced by this UTMF electrode, the derived MCPSC possessed a high translational factor of ≈74% when its active area was scaled up from 0.2 cm^2 (PCE: 4.16%) to 25 cm^2 (3.08%). In contrast, the control ITO device that had an inferior translational factor of ≈32%; the PCE dropped from 5.48% (0.2 cm^2) to 1.75% (25 cm^2) due to the high R_S (15–20 Ω □$^{-1}$) of ITO (Figure 13b).

Lately, Yun et al. reported a high-performance flexible MCPSC based on ZnO–AgO_X–ZnO (ZAOZ) transparent conducting electrode (TCE) as displayed in **Figure 14**a.[120] They showed that slight oxidation of the central Ag UTMF (denoted as AgO_X) facilitated homogeneous thin-film formation on ZnO due to improved wettability. Accordingly, a reduced percolation threshold as low as 6 nm was achieved for the AgO_X UTMF. This enabled the optimized ZAOZ TCE to possess an improved transmittance across the entire visible spectrum (average transmittance (AT) of 91% across the spectral range of 400–1000 nm without sacrificing electrical conductivity (20 Ω □$^{-1}$) compared to the ZnO–Ag–ZnO (ZAZ) TCE comprising of a 6 nm Ag UTMF with a granular morphology. Consequently, the optimized ZAOZ TCE yielded an efficient (PCE: 6.34%) flexible MCPSC, exceeding the performance (5.65%) of the ZAZ UTMF based MCPSCs (Figure 14a). In addition, the MCPSCs exhibited remarkable bending durability due to the excellent ductility of Ag-based UTMFs.

Taking a different tack, Jen et al. engineered the interfaces of the ZAZ TCE with functional self-assembled monolayers (SAMs) to fabricate efficient, flexible, stable, and ITO-free PSCs.[121] As illustrated in Figure 14b, a double-ended functionalized organic SAM, 11-mercapto-undecanoic acid (MUA), was first attached covalently onto the ZnO seeding layer to serve as

a molecular binder. The terminal thiol group bonded with Ag, while the carboxylic acid reacted with the hydroxyl group on the ZnO surface to form an ester linkage. Owing to the improved compatibility with the molten Ag introduced by the MUA SAM, the surface diffusion of Ag on ZnO was reduced, thus facilitating the nucleation and growth of the Ag UTMF. Consequently, a 10 nm Ag UTMF had a smooth surface (root-mean-square roughness: ≈0.95 nm) and low R_S (8.6 and 9.0 Ω □$^{-1}$ on glass and polyethylene naphthalate substrates, respectively). Furthermore, the MUA SAM was used to modify the other Ag/ZnO interface (the other ZnO layer served as an ETL) to enable improved interfacial adhesion and energy level alignment, facilitating charge extraction from the organic absorbers. Finally, the surface of ZnO ETL was modified with a C_{60}-based SAM to passivate surface traps, which enhanced the electronic coupling and charge selectivity between the ZnO ETL and the active layer.[122] Given these advantages, this SAM-modified ZAZ TCE enabled an efficient (average PCE of 6.00%), flexible MCPSC based on PIDT-PhanQ:PC_{71}BM BHJ with superior mechanical stability to the pristine ITO device (average PCE of 5.49%).

In addition to the MoO_3 and ZnO TMOs, Guo and Liu et al. developed WO_3/Ag/WO_3 (WAW) and NiO/Ag/NiO (NAN) TCEs to fabricate stable and high-performance flexible MCPSCs.[123,124] They reported that both WO_3 and NiO behaved as effective seeding layers for high quality Ag UTMFs (10–11 nm) with decent optical and electrical properties on both rigid ITO and flexible substrates. The optimized WAW electrode had an AT of 82.6% over a spectral range of 350–700 nm (cf. 84.2% for ITO over the same range) with a low R_S of ≈9 Ω □$^{-1}$ on glass, while the optimized NAN TCE showed a slightly lower AT of 77% over 400–700 nm (cf. 79% for ITO over the same range) with a low R_S of ≈7.6 Ω □$^{-1}$ on a polyethylene terephthalate (PET) substrate. Moreover, WO_3 and NiO (the other TMO layer in the composite TCE) also served as efficient HTLs and modify the WF of the derived TCE to provide better energy level alignment at the electrode/BHJ interface, facilitating charge extraction in the device. As a result, the derived flexible MCPSCs not only possessed PCEs superior to those of the regular ITO devices but also exhibited much improved mechanical and environmental stability.

As mentioned above, the organic-based D/M/D TCEs have also been exploited in recent years. Lee et al. first demonstrated a BCP/Ag/MoO_3 electrode to build a top-illuminated PSC.[108] They showed that the MoO_3 with a high refractive index ($\eta \approx 2.0$) served as an efficient light in-coupling layer for Ag UTMFs, while the BCP layer functioned as a seeding layer and ETL simultaneously. The resultant BCP/Ag/MoO_3 TCE achieved the optimal zero-reflection condition, leading to its high optical transparency (>75% in the visible region, 400–700 nm) and low R_S (≈8.6–9 Ω □$^{-1}$) (**Figure 15**a). Lin et al. followed by employing a similar BCP/Ag/MoO_3 TCE to fabricate high-performance microcavity small molecule organic solar cells (SMOSCs).[42] As shown in Figure 15b, they revealed that the optical-field distribution inside the device had a strong correlation with both the in-cell optical spacer layer (an MoO_3 HTL in this case) and the out-of-cell capping layer (LiF, $\eta \approx 1.4$; or MoO_3, $\eta \approx 2.1$). They concluded that the transparent capping layer with a higher refractive index could result in a higher efficiency of the derived device. The flexible SMOSC yielded a PCE of 5%, comparable to that of the reference ITO device. More encouragingly, scaling up the device area from 5 mm^2 to 36 mm^2 resulted in only a slight efficiency loss of ≈4% (PCE: 4.8%).

In the meanwhile, Jen et al. used another high refractive index material, TeO_2 ($\eta \approx 2.15$), as an effective capping layer to fabricate highly efficient MCPSCs both in bottom- and top-illuminated configurations.[43,113] A TeO_2/Ag/PEDOT:PSS TCE was first developed and utilized in a bottom-illuminated MCPSC (**Figure 16**a).[43] In this structure, the TeO_2 also functioned as a seeding layer to facilitate the growth of Ag UTMF for high conductivity and optical transparency. For example, a 12 nm-thick Ag UTMF deposited on TeO_2 possessed a low R_S of 7.02 Ω □$^{-1}$ and an AT of 54.89% in the wavelength range of 330–800 nm. The importance of the refractive index and thickness of this capping layer on device performance was

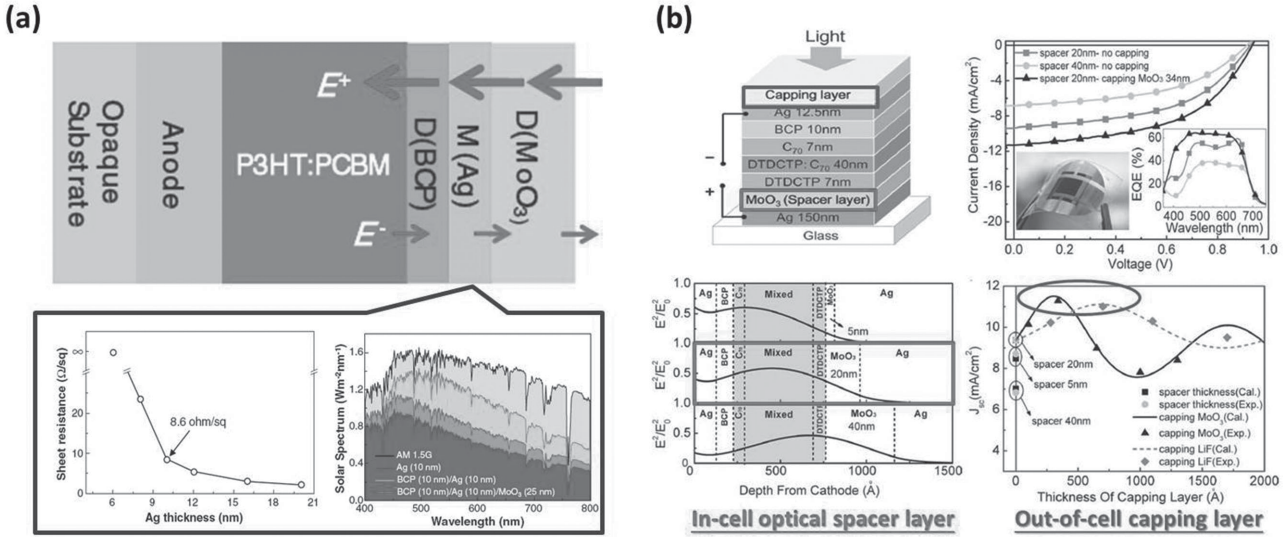

Figure 15. a) Schematic of the electric field propagation in a BCP/Ag/MoO_3 TCE and its R_S and optical transmittance. b) BCP/Ag/MoO_3 UTMF based SMOSC. a) Adapted with permission.[108] b) Adapted with permission.[42]

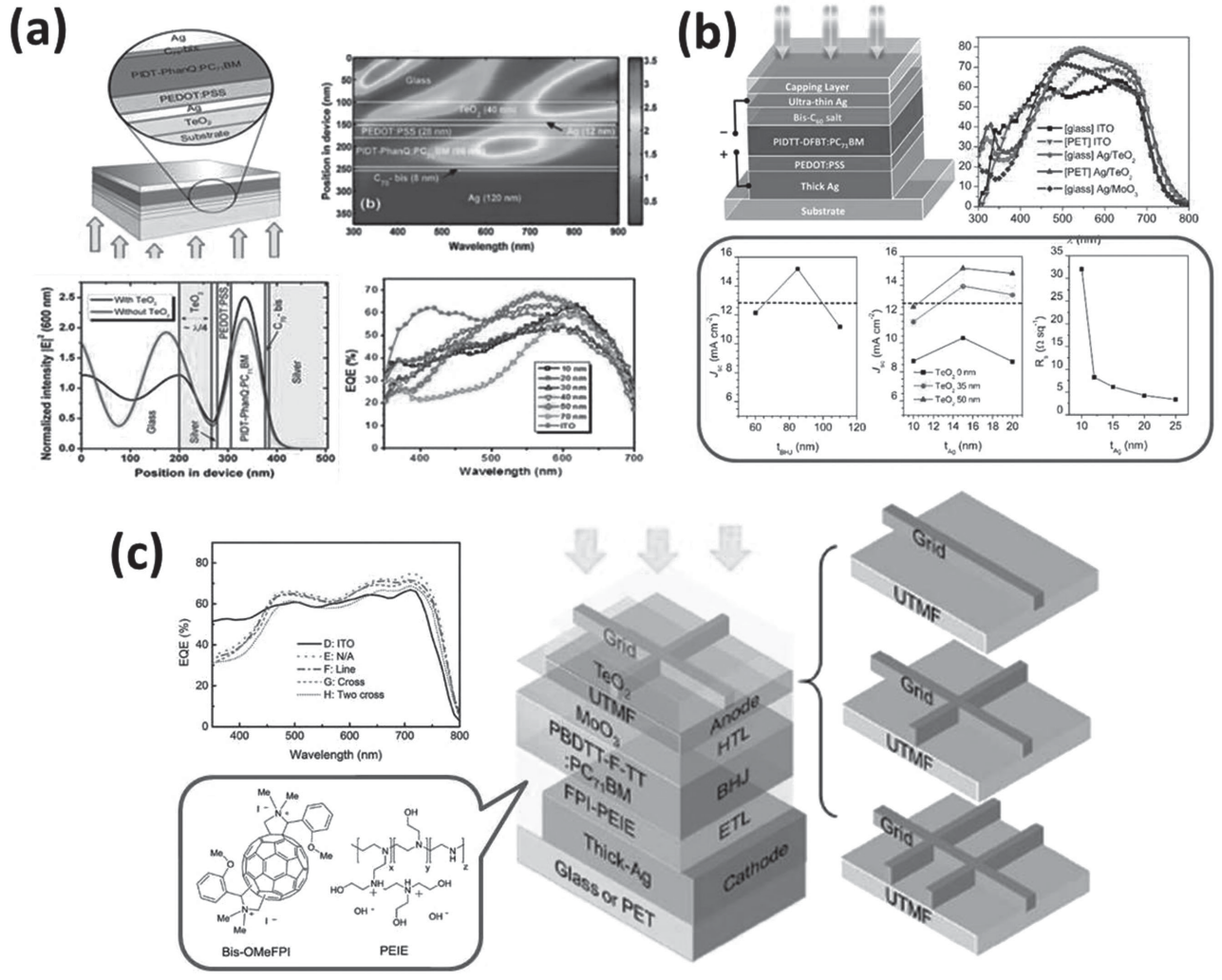

Figure 16. a) Bottom-illuminated MCPSC with a TeO_2/Ag/PEDOT:PSS TCE and top-illuminated MCPSCs with b) TeO_2/Ag/Bis-C_{60} and c) TeO_2/Ag/MoO_3 TCEs, respectively. a) Adapted with permission.[43] b) Adapted with permission.[113] c) Adapted with permission.[125]

revealed. By comparing MoO_3 ($\eta \approx 1.75$) and TeO_2 ($\eta \approx 2.15$), we showed that the optimized TeO_2 capping layer yielded an increased photocurrent of the derived resonant microcavity, consistent with the trend reported by Lin et al., and our results indicated that the thickness of this out-of-cell TeO_2 layer influenced the optical distribution inside the device. MCPSCs based on PIDT-PhanQ:$PC_{71}BM$ BHJ yielded slightly higher PCEs than the control ITO devices on both glass ($PCE_{TeO2/Ag}$ = 6.6%, PCE_{ITO} = 6.5%) and plastic ($PCE_{TeO2/Ag}$ = 5.8%, PCE_{ITO} = 5.6%) substrates.

Afterward, Jen et al. explored another TeO_2-based TCE (TeO_2/Ag/Bis-C_{60}) to fabricate a top-illuminated MCPSC with improved light-trapping efficiency, as illustrated in Figure 16b.[113] The influence of the thickness of the in-cell BHJ layer and the out-of-cell TeO_2 capping layer on the resultant microcavity resonance effects were investigated systematically. Once again, the higher refractive index of TeO_2 compared to that of MoO_3 afforded a higher J_{SC} for the derived MCPSC. Due to prominent microcavity resonance effects, the enhanced light-trapping inside the devices boosted the J_{SC} in PIDTT-DFBT:$PC_{71}BM$ BHJ MCPSCs, leading to improved PCEs on both glass ($PCE_{TeO2/Ag}$ = 8.5%, PCE_{ITO} = 7.2%) and plastic ($PCE_{TeO2/Ag}$ = 8.4%, PCE_{ITO} = 6.6%) substrates. These results also indicated the microcavity configuration in the top-illuminated architecture played a more essential role in device operation than in the bottom-illuminated architecture. Recently, we modified this top-illuminated microcavity configuration with a more conductive fullerene ETL (FPI-PEIE) and integrated it with a more efficient PBDTT-F-TT:$PC_{71}BM$ BHJ system to yield a high PCE of 10.4% (Figure 16c), which represented 11% and 10% enhancements in J_{SC} and PCE, respectively, compared to the control ITO device.[125] Moreover, the TCE MoO_3/Ag/TeO_2 modified with semitransparent metal grids was incorporated to realize a high PCE of 7.21% in large active-area (1 cm^2) devices (Figure 16c), representing a 26% enhancement in PCE compared to the large-area ITO device. The improved PCE in the large-area device was attributed to the superior conductivity and comparable transparency of the UTMF. These results signify the great potential of high-performance, large-area, and flexible MCPSCs for future commercialization.

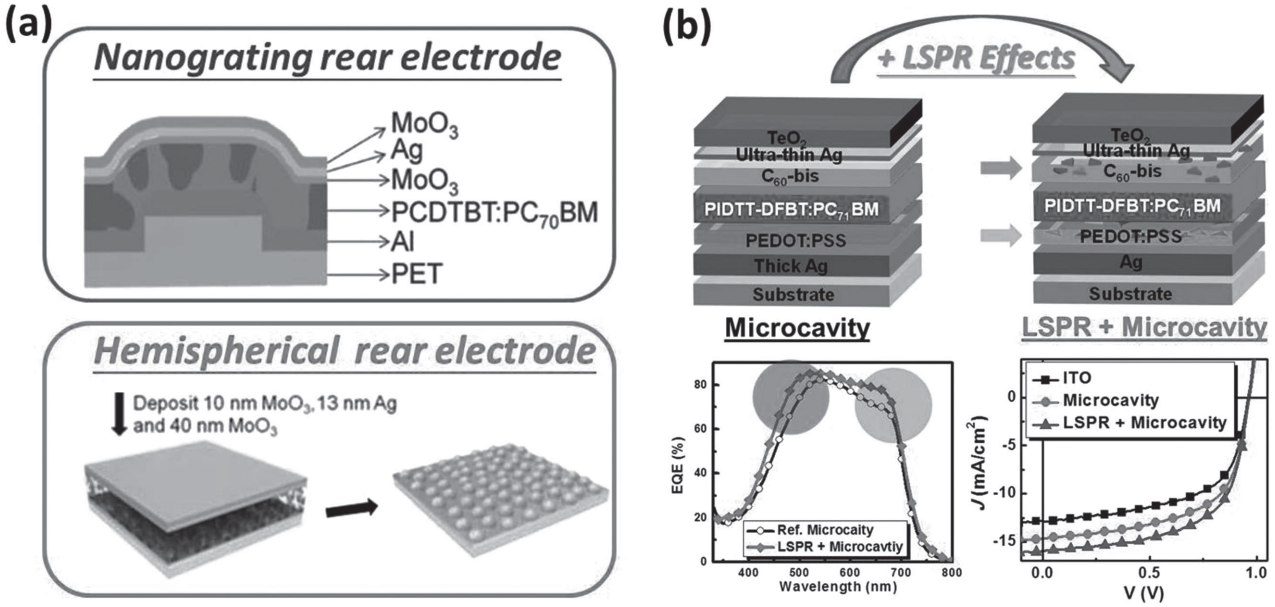

Figure 17. a) Top-illuminated MCPSCs with nanostructured rear electrodes. b) Top-illuminated MCPSCs with metal NP-embedded CTLs that induce LSPR effects. a) (top) Adapted with permission.[127] Copyright 2014, The Royal Society of Chemistry. a) (bottom) Adapted with permission.[126] b) Adapted with permission.[128]

Intriguingly, SPR effects have been coupled with the microcavity configuration to achieve enhanced broadband absorption in PSCs.[126–128] Jung et al. have modified the opaque rear metal electrode with nanogratings or hemispherical nanoarrays to introduce scattering and SPR effects into top-illuminated MSPSC (**Figure 17**a).[126,127] They showed that not only did the nanostructured backside electrodes enhance absorption via scattering and SPR effects, but also the increased interfaces between the nanostructured electrode and BHJ layer facilitated charge collection efficiency. However, these nanostructured electrodes deteriorated film reflectivity and the resultant microcavity resonance effects in the derived devices, suggesting that this may not be the best approach to integrate SPR effects into a microcavity configuration.

Hence, Jen et al. recently induced LSPR effects into the microcavity structure by embedding metal NPs into both the ETL and HTL of the devices[128] as done in their previous reports.[53,54] These NP-embedded CTLs were incorporated into a top-illuminated MCPSC to combine LSPR and microcavity resonance effects in a synergistic manner, enabling the broadband optical enhancement illustrated in Figure 17b. Consequently, a high-performance (PCE ≈ 9.4%), ITO-free, and flexible MCPSC based on PIDTT-DFBT:PC_{71}BM BHJ was demonstrated.[128] More intriguingly, the resonant wavelengths of the plasmonic effects introduced by the metal NPs could be tuned by carefully controlling NP size and doping position in the device to increase complementary light harvesting.

4.3.2. Multi-Junction Tandem Solar Cells

Based on Kirchhoff's junction rule, imbalanced J_{SC} contributions between constituent subcells of a series-connected tandem device limit device PCE. Ensuring balanced J_{SC}s contributions necessitates careful manipulation of the optical field in each constituent subcell. With this optoelectronic requirement in mind, microcavity configurations have been adopted into tandem architectures to manage the optical distribution within each constituent subcells. Kim et al. first evaluated the efficacy of the microcavity configuration in a tandem device with TMM optical simulation.[129] They demonstrated that microcavity resonance effects can enable a 25% increased J_{SC} in the tandem SMOSC compared to an ITO-based counterpart by controlling the optimized thicknesses of both the in-cell optical spacer layer (i.e., CTLs) and the out-of-cell capping layers of the TCE (BCP/Ag/Alq_3).

Feng and Sun et al. followed by experimentally verifying this J_{SC} enhancement in a similar microcavity-embedded tandem SMOSC that integrated SPP effects,[130] where a periodically corrugated microcavity tandem architecture was introduced to match current contributions between the subcells, optimizing the resultant J_{SC} and PCE (**Figure 18**a).[130] They revealed strong interference between the SPP and microcavity modes occurring at the backside Ag/BHJ interface (Figure 18b) and demonstrated that this anti-crossing effect can enhance the light harvesting of the rear subcell to yield a more balanced photocurrent with the front subcell. Consequently, 10.4% and 11.3% enhancements in the resultant J_{SC} and PCE of the derived device were achieved as compared to the planar microcavity device.

As discussed previously, microcavity resonance effects will diminish as the length of the chamber gradually increases. Therefore, instead of fabricating a microcavity tandem structure with a long chamber across the constituent subcells, the UTMF was recently employed as an interconnection layer (ICL) in the tandem device to form a microcavity within the subcell. This mirror-like ICL manipulates the reciprocity between reflection and transmission of incoming light to

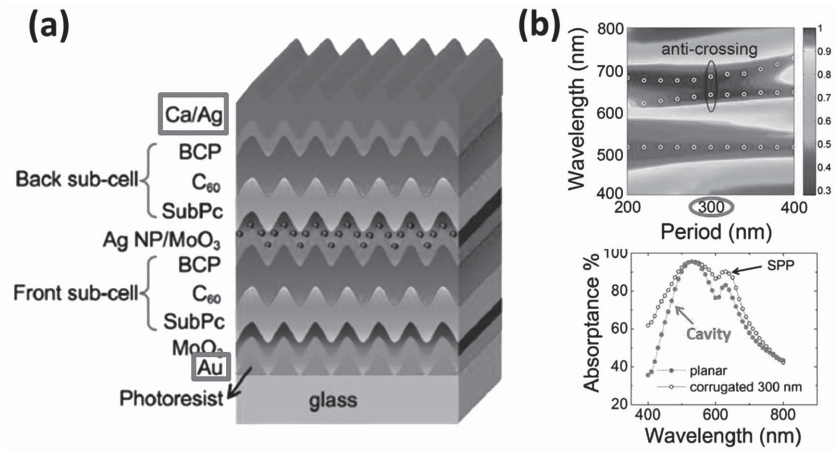

Figure 18. a) Device structure of the corrugated microcavity tandem SMOSC. b) (top) The dispersion relationship for the wavelength versus the period of the corrugation of the corrugated tandem devices. (bottom) The experimentally measured absorption spectra of the planar and corrugated tandem device with periods of 300 nm. Adapted with permission.[130]

modulate the optical distribution inside the tandem device, providing better photocurrent matching between the subcells. More importantly, this UTMF ICL can either serve as an excellent charge recombination site for a series-connected tandem device or as an intermediate electrode to construct a three-terminal parallel-connected tandem cell. Recently, Long et al. evaluated the efficacy of a WO_3/Ag/WO_3 ICL in a parallel-connected tandem structure by TMM optical modeling.[131] Encouragingly, their results suggested that a microcavity in the rear subcell could shift the absorption spectrum of the rear cell to match the minimum absorption of the front cell, facilitating complementary absorption and increasing total absorption in the tandem cell.

As mentioned previously, the active layer of the front subcell of an optimal tandem device should possess a relatively large E_g to absorb high-energy photons, while the active layer of the rear subcell should have relatively a low E_g to absorb transmitted low-energy photons. This architecture minimizes thermalization loss in the low-E_g subcell, increasing the V_{OC} and PCE of the derived tandem device. Simulation results reported by Long et al.[131] indicated that the transmitted photons near the absorption band edge (usually close to NIR region) of the front subcell could be trapped and reabsorbed in the rear subcell as a result of the formed microcavity inside, suggesting that using a UTMF as an ICL can help reduce the absorption overlap between the constituent subcells, providing a more balanced J_{SC} from each subcell. A 80% improvement in the NIR absorption was realized in the microcavity-embedded rear subcell, thereby leading to a 17.8% enhancement in the TAP within the entire tandem device (λ = 400–900 nm).

Recently, Jen et al. independently reported this enhanced light-trapping in microcavity tandem devices and realized impressive, high-performance parallel- and series-connected tandem PCSs with PCEs of 9.2% and ≈11%, respectively.[132,133] The MoO_3/Ag/PEDOT:PSS TCE was utilized as an intermediate electrode to combine a semitransparent device with a top-illuminated MCPSC in a parallel-connected tandem PSC architecture, as illustrated in **Figure 19**a.[133] The EQE of the individual subcells was measured to determine the individual photocurrents and demonstrate the advantage of embedding a microcavity structure into the rear subcell. The EQE results indicated that microcavity-embedded rear subcells could improve the absorption of low energy photons near the absorption band edge of the BHJ layer to improve the light-trapping in the tandem architecture, increasing the tandem J_{SC} (Figure 19b), which experimentally supported the hypothesis made by Long et al.[131]

Shortly, a novel MoO_3/Ag/PFN ICL with cascaded energy levels was designed to establish a high-performance series-connected

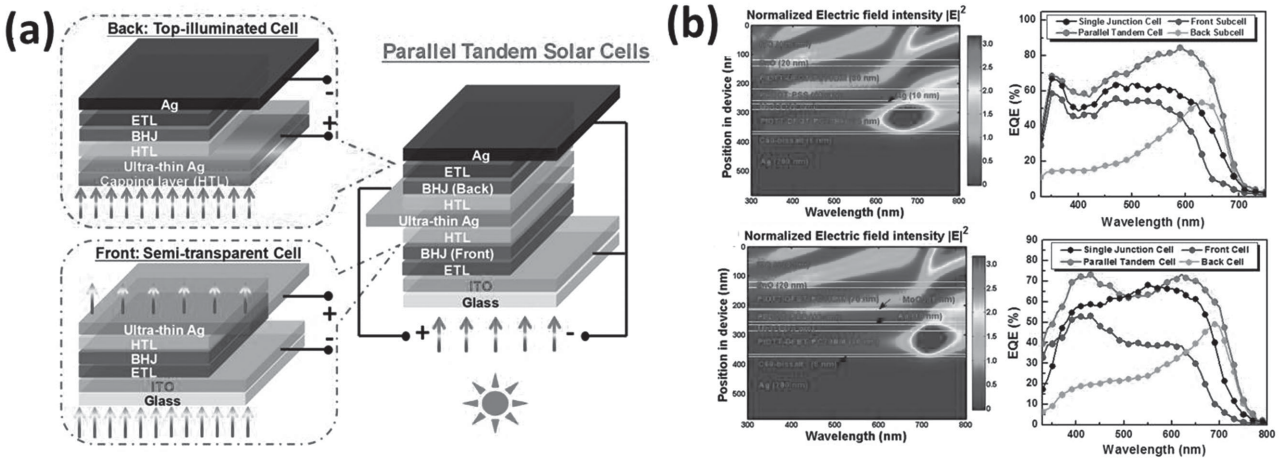

Figure 19. a) Schematic of the parallel-connected microcavity tandem PSC. b) Light intensity distribution in the parallel-connected microcavity tandem devices with various BHJ systems and their experimental EQE spectra in comparison with those of the reference single cell and the constituent subcells. Adapted with permission.[133]

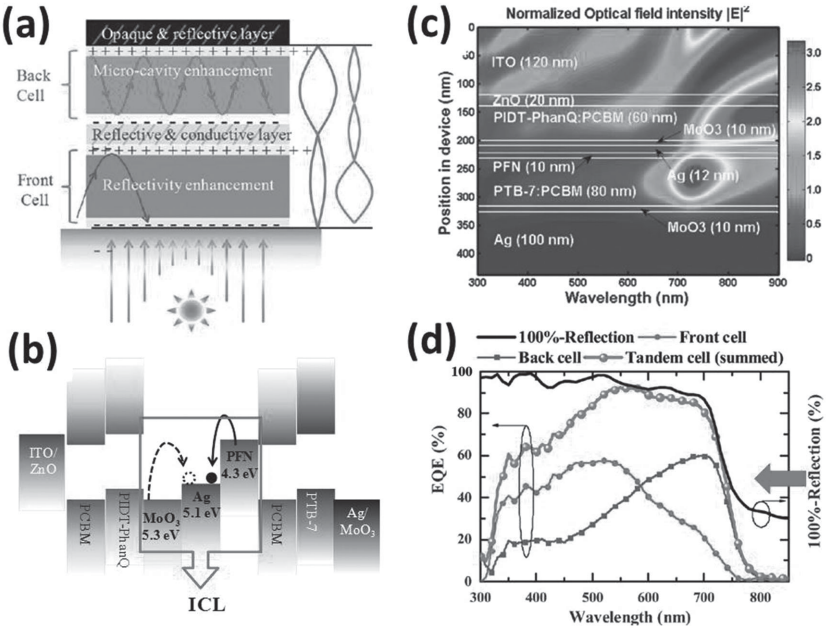

Figure 20. a) Schematic of the series-connected microcavity tandem PSC and b) its energy level diagram. c) Light intensity distribution in the series-connected microcavity tandem devices. d) EQE spectrum of the front cell (green line), the back cell (blue), the summed EQE spectrum of both subcells (red), and 100%-reflection spectrum of the tandem device (black). Adapted with permission.[132] Copyright 2015, The Royal Society of Chemistry.

tandem PCS, as present in **Figure 20**a,b[132] In addition to serving as an efficient charge extraction and recombination site, this mirror-like ICL further optimized the distribution of optical field inside the tandem device to achieve balanced J_{SC}s between the subcells. Similar to the case of the parallel-connected tandem PSC, the superior reflective transparent properties of this novel ICL formed a microcavity structure with the back subcell to enhance the overall light confinement inside the tandem device. Consequently, the derived tandem PCS yielded a promising PCE of ≈11% with a maximum summed EQE peak value over 90%. These results validate the efficacy of microcavity resonance effects in tandem devices, providing a new strategy for further improvements in the photovoltaic performance of tandem PSCs.

5. Conclusion and Outlook

We have comprehensively reviewed recent progress in PSC electrode engineering. To date, various nanostructured and planar electrode designs have been exploited to enhance the light-trapping in devices through distinct plasmon resonance mechanisms. Planar UTMFs particularly have attracted significant attention due to their remarkably reflective transparent properties that are necessary to form an efficient optical microcavity in the device.

This microcavity configuration has a much stronger effect in devices with a relatively thin (<100 nm, usually) organic absorbing layer. Resonant microcavity effects enable the photocurrent of thin-film PSCs to reach the high values observed in thick-film devices, which is noteworthy considering the short exciton diffusion lengths and low carrier mobilities observed in thin-film PSCs relative to their inorganic counterparts. To further improve the photovoltaic performance of MCPSCs, deeper understanding of the optical mechanisms arising from the microcavity configuration is required, especially for the tandem architectures. As revealed earlier, using an UTMF as an ICL or an intermediate electrode in three-terminal tandem PSCs not only can modulate the optical field distribution in each subcell to ensure balanced J_{SC} contributions but also can allow for direct measurement of the light harvesting behavior of each subcell. A more detailed investigation of the relationship between the thickness of the UTMF ICL and the resulting optical field distribution in constituent subcell will elucidate this issue. Also, the interplay between the thickness of the out-of-cell capping layer and the optical density inside the device must be evaluated to optimize the light-trapping in the device.

In addition, the angular dependence of incident light in MCPSCs warrants further investigation. For example, Shtein et al. have recently demonstrated that the SPR effects induced by the planar electrodes vary as a function of the angle of the incident light, which affects the range of optical enhancement realized from a given resonant cavity.[134] Therefore, understanding the angular selectivity of the microcavity structure requires more fundamental studies.

Recently, semi-transparent PSCs have attracted much research interest because of their potential to serve as power-generating windows for buildings and automobiles. In this regard, developing a microcavity-embedded semi-transparent PSC will be a good strategy to further enhance its performance. By manipulating the off resonance and the microcavity resonance in the device, we can modulate the spectral region of incident light to be converted into electric power to optimize both the resultant transmittance and photovoltaic performance; Martorell and coworkers recently reported a proof-of-concept study.[135] In addition, microcavity structures also can be employed as an efficient backside reflector in semi-transparent PSCs to modulate the light trapping and transmittance of the devices.[136] The colors of the semi-transparent PSCs can be tuned by varying the thickness of the optical spacers sandwiched in the backside cavity structure, which adds the aesthetic value of semi-transparent PSCs in future commercial applications.

Acknowledgements

This work is supported by the Office of Naval Research (N00014-14-1-0170) and the Asian Office of Aerospace R&D (FA2386-11-1-4072). A. K.-Y. Jen thanks the Boeing-Johnson Foundation for financial support.

Received: August 18, 2015
Revised: October 12, 2015
Published online: December 7, 2015

[1] M. C. Scharber, N. S. Sariciftci, *Prog. Polym. Sci.* **2013**, *38*, 1929.
[2] J. You, L. Dou, Z. Hong, G. Li, Y. Yang, *Prog. Polym. Sci.* **2013**, *38*, 1909.
[3] S.-H. Liao, H.-J. Jhuo, P.-N. Yeh, Y.-S. Cheng, Y.-L. Li, Y.-H. Lee, S. Sharma, S.-A. Chen, *Sci. Rep.* **2014**, *4*.
[4] J.-D. Chen, C. Cui, Y.-Q. Li, L. Zhou, Q.-D. Ou, C. Li, Y. Li, J.-X. Tang, *Adv. Mater.* **2015**, *27*, 1035.
[5] A. R. b. M. Yusoff, D. Kim, H. P. Kim, F. K. Shneider, W. J. da Silva, J. Jang, *Energy Environ. Sci.* **2015**, *8*, 303.
[6] Y.-J. Cheng, S.-H. Yang, C.-S. Hsu, *Chem. Rev* **2009**, *109*, 5868.
[7] A. Haugeneder, M. Neges, C. Kallinger, W. Spirkl, U. Lemmer, J. Feldmann, U. Scherf, E. Harth, A. Gügel, K. Müllen, *Phys. Rev B* **1999**, *59*, 15346.
[8] M. Theander, A. Yartsev, D. Zigmantas, V. Sundström, W. Mammo, M. R. Andersson, O. Inganäs, *Phys. Rev B* **2000**, *61*, 12957.
[9] X. Guo, N. Zhou, S. J. Lou, J. Smith, D. B. Tice, J. W. Hennek, R. P. Ortiz, J. T. L. Navarrete, S. Li, J. Strzalka, L. X. Chen, R. P. H. Chang, A. Facchetti, T. J. Marks, *Nat. Photon.* **2013**, *7*, 825.
[10] S. H. Park, A. Roy, S. Beaupre, S. Cho, N. Coates, J. S. Moon, D. Moses, M. Leclerc, K. Lee, A. J. Heeger, *Nat. Photon.* **2009**, *3*, 297.
[11] W. Li, K. H. Hendriks, W. S. C. Roelofs, Y. Kim, M. M. Wienk, R. A. J. Janssen, *Adv. Mater.* **2013**, *25*, 3182.
[12] J. Cao, Q. Liao, X. Du, J. Chen, Z. Xiao, Q. Zuo, L. Ding, *Energy Environ. Sci.* **2013**, *6*, 3224.
[13] X. Hu, C. Yi, M. Wang, C.-H. Hsu, S. Liu, K. Zhang, C. Zhong, F. Huang, X. Gong, Y. Cao, *Adv. Energy Mater.* **2014**, *4*, 1400378.
[14] T. L. Nguyen, H. Choi, S. J. Ko, M. A. Uddin, B. Walker, S. Yum, J. E. Jeong, M. H. Yun, T. J. Shin, S. Hwang, J. Y. Kim, H. Y. Woo, *Energy Environ. Sci.* **2014**, *7*, 3040.
[15] R. Kroon, A. Diaz de Zerio Mendaza, S. Himmelberger, J. Bergqvist, O. Bäcke, G. C. Faria, F. Gao, A. Obaid, W. Zhuang, D. Gedefaw, E. Olsson, O. Inganäs, A. Salleo, C. Müller, M. R. Andersson, *J. Am. Chem. Soc.* **2014**, *136*, 11578.
[16] W. Li, S. Albrecht, L. Yang, S. Roland, J. R. Tumbleston, T. McAfee, L. Yan, M. A. Kelly, H. Ade, D. Neher, W. You, *J. Am. Chem. Soc.* **2014**, *136*, 15566.
[17] S. Basu Mallick, N. P. Sergeant, M. Agrawal, J.-Y. Lee, P. Peumans, *MRS Bull.* **2011**, *36*, 453.
[18] Z. Tang, W. Tress, O. Inganäs, *Mater. Today* **2014**, *17*, 389.
[19] W. Cao, J. Xue, *Energy Environ. Sci.* **2014**, *7*, 2123.
[20] J. D. Myers, W. Cao, V. Cassidy, S.-H. Eom, R. Zhou, L. Yang, W. You, J. Xue, *Energy Environ. Sci.* **2012**, *5*, 6900-.
[21] S. Esiner, T. Bus, M. M. Wienk, K. Hermans, R. A. J. Janssen, *Adv. Energy Mater.* **2013**, *3*, 1013.
[22] J.-D. Chen, L. Zhou, Q.-D. Ou, Y.-Q. Li, S. Shen, S.-T. Lee, J.-X. Tang, *Adv. Energy Mater.* **2014**, *4*, 1301777.
[23] L. A. A. Pettersson, L. S. Roman, O. Inganäs, *J. Appl. Phys.* **1999**, *86*, 487.
[24] J. Y. Kim, S. H. Kim, H. H. Lee, K. Lee, W. Ma, X. Gong, A. J. Heeger, *Adv. Mater.* **2006**, *18*, 572.
[25] J. Gilot, I. Barbu, M. M. Wienk, R. A. J. Janssen, *Applied Physics Letters* **2007**, *91*, 113520.
[26] A. Hadipour, D. Cheyns, P. Heremans, B. P. Rand, *Adv. Energy Mater.* **2011**, *1*, 930.
[27] A. K. K. Kyaw, D. H. Wang, D. Wynands, J. Zhang, T.-Q. Nguyen, G. C. Bazan, A. J. Heeger, *Nano Lett.* **2013**, *13*, 3796.
[28] C.-C. Chueh, S.-C. Chien, H.-L. Yip, J. F. Salinas, C.-Z. Li, K.-S. Chen, F.-C. Chen, W.-C. Chen, A. K. Y. Jen, *Adv. Energy Mater.* **2013**, *3*, 417.
[29] T. Ameri, N. Li, C. J. Brabec, *Energy Environ. Sci.* **2013**, *6*, 2390.
[30] H. Zhou, Y. Zhang, C.-K. Mai, S. D. Collins, G. C. Bazan, T.-Q. Nguyen, A. J. Heeger, *Adv. Mater.* **2015**, *27*, 1767.
[31] K. S. Nalwa, J.-M. Park, K.-M. Ho, S. Chaudhary, *Adv. Mater.* **2011**, *23*, 112.
[32] L. Müller-Meskamp, Y. H. Kim, T. Roch, S. Hofmann, R. Scholz, S. Eckardt, K. Leo, A. F. Lasagni, *Adv. Mater.* **2012**, *24*, 906.
[33] J. B. Kim, P. Kim, N. C. Pegard, S. J. Oh, C. R. Kagan, J. W. Fleischer, H. A. Stone, Y.-L. Loo, *Nat. Photon.* **2012**, *6*, 327.
[34] R. Betancur, P. Romero-Gomez, A. Martinez-Otero, X. Elias, M. Maymo, J. Martorell, *Nat. Photon.* **2013**, *7*, 995.
[35] H. A. Atwater, A. Polman, *Nat. Mater.* **2010**, *9*, 205.
[36] Q. Gan, F. J. Bartoli, Z. H. Kafafi, *Adv. Mater.* **2013**, *25*, 2385.
[37] C.-H. Chou, F.-C. Chen, *Nanoscale* **2014**, *6*, 8444.
[38] W. C. H. Choy, *Chem. Commun.* **2014**, *50*, 11984.
[39] W. C. H. Choy, W. K. Chan, Y. Yuan, *Adv. Mater.* **2014**, *26*, 5368.
[40] J. Lee, S.-Y. Kim, C. Kim, J.-J. Kim, *Appl. Phys. Lett.* **2010**, *97*, 083306.
[41] N. P. Sergeant, A. Hadipour, B. Niesen, D. Cheyns, P. Heremans, P. Peumans, B. P. Rand, *Adv. Mater.* **2012**, *24*, 728.
[42] H.-W. Lin, S.-W. Chiu, L.-Y. Lin, Z.-Y. Hung, Y.-H. Chen, F. Lin, K.-T. Wong, *Adv. Mater.* **2012**, *24*, 2269.
[43] J.-F. Salinas, H.-L. Yip, C.-C. Chueh, C.-Z. Li, J.-L. Maldonado, A. K. Y. Jen, *Adv. Mater.* **2012**, *24*, 6362.
[44] D. H. Wang, D. Y. Kim, K. W. Choi, J. H. Seo, S. H. Im, J. H. Park, O. O. Park, A. J. Heeger, *Angew. Chem., Int. Ed.* **2011**, *50*, 5519.
[45] J. Yang, J. You, C.-C. Chen, W.-C. Hsu, H.-r. Tan, X. W. Zhang, Z. Hong, Y. Yang, *ACS Nano* **2011**, *5*, 6210.
[46] R. B. Dunbar, H. C. Hesse, D. S. Lembke, L. Schmidt-Mende, *Phys. Rev B* **2012**, *85*, 035301.
[47] X. Li, W. C. H. Choy, H. Lu, W. E. I. Sha, A. H. P. Ho, *Adv. Funct. Mater.* **2013**, *23*, 2728.
[48] H. Choi, S.-J. Ko, Y. Choi, P. Joo, T. Kim, B. R. Lee, J.-W. Jung, H. J. Choi, M. Cha, J.-R. Jeong, I.-W. Hwang, M. H. Song, B.-S. Kim, J. Y. Kim, *Nat. Photon.* **2013**, *7*, 732.
[49] S.-J. Ko, H. Choi, W. Lee, T. Kim, B. R. Lee, J.-W. Jung, J.-R. Jeong, M. H. Song, J. C. Lee, H. Y. Woo, J. Y. Kim, *Energy Environ. Sci.* **2013**, *6*, 1949.
[50] S.-W. Baek, G. Park, J. Noh, C. Cho, C.-H. Lee, M.-K. Seo, H. Song, J.-Y. Lee, *ACS Nano* **2014**, *8*, 3302.
[51] H. Choi, J.-P. Lee, S.-J. Ko, J.-W. Jung, H. Park, S. Yoo, O. Park, J.-R. Jeong, S. Park, J. Y. Kim, *Nano Lett.* **2013**, *13*, 2204.
[52] X. Li, W. C. H. Choy, L. Huo, F. Xie, W. E. I. Sha, B. Ding, X. Guo, Y. Li, J. Hou, J. You, Y. Yang, *Adv. Mater.* **2012**, *24*, 3046.
[53] X. Yang, C.-C. Chueh, C.-Z. Li, H.-L. Yip, P. Yin, H. Chen, W.-C. Chen, A. K. Y. Jen, *Adv. Energy Mater.* **2013**, *3*, 666.
[54] K. Yao, M. Salvador, C.-C. Chueh, X.-K. Xin, Y.-X. Xu, D. W. deQuilettes, T. Hu, Y. Chen, D. S. Ginger, A. K. Y. Jen, *Adv. Energy Mater.* **2014**, *4*, 1400206.
[55] H. R. Yeom, J. Heo, G.-H. Kim, S.-J. Ko, S. Song, Y. Jo, D. S. Kim, B. Walker, J. Y. Kim, *Phys. Chem. Chem. Phys.* **2015**, *17*, 2152.
[56] C. E. Petoukhoff, Z. Shen, M. Jain, A. Chang, D. M. O'Carroll, *PHOTOE* **2015**, *5*, 057002.
[57] H. J. Park, T. Xu, J. Y. Lee, A. Ledbetter, L. J. Guo, *ACS Nano* **2011**, *5*, 7055.
[58] C. Min, J. Li, G. Veronis, J.-Y. Lee, S. Fan, P. Peumans, *Appl. Phys. Lett.* **2010**, *96*, 133302.
[59] L. Stolz Roman, O. Inganäs, T. Granlund, T. Nyberg, M. Svensson, M. R. Andersson, J. C. Hummelen, *Adv. Mater.* **2000**, *12*, 189.
[60] K. Tvingstedt, N.-K. Persson, O. Inganäs, A. Rahachou, I. V. Zozoulenko, *Appl. Phys. Lett.* **2007**, *91*, 113514.
[61] M. A. Sefunc, A. K. Okyay, H. V. Demir, *Opt. Express* **2011**, *19*, 14200.
[62] J. You, X. Li, F.-x. Xie, W. E. I. Sha, J. H. W. Kwong, G. Li, W. C. H. Choy, Y. Yang, *Adv. Energy Mater.* **2012**, *2*, 1203.
[63] H. Shen, B. Maes, *Opt. Express* **2011**, *19*, A1202.
[64] X. Li, W. C. H. Choy, X. Ren, J. Xin, P. Lin, D. C. W. Leung, *Appl. Phys. Lett.* **2013**, *102*, 153304.
[65] X. H. Li, W. E. I. Sha, W. C. H. Choy, D. D. S. Fung, F. X. Xie, *J. Phys. Chem. C* **2012**, *116*, 7200.
[66] W. E. I. Sha, W. C. H. Choy, W. C. Chew, *Opt. Express* **2010**, *18*, 5993.
[67] D. H. Wang, J. Seifter, J. H. Park, D.-G. Choi, A. J. Heeger, *Adv. Energy Mater.* **2012**, *2*, 1319.

[68] B. Wu, T. Z. Oo, X. Li, X. Liu, X. Wu, E. K. L. Yeow, H. J. Fan, N. Mathews, T. C. Sum, *J. Phys. Chem. C* **2012**, *116*, 14820.
[69] A. Kirkeminde, M. Retsch, Q. Wang, G. Xu, R. Hui, J. Wu, S. Ren, *Nanoscale* **2012**, *4*, 4421.
[70] L. Zhou, Q.-D. Ou, J.-D. Chen, S. Shen, J.-X. Tang, Y.-Q. Li, S.-T. Lee, *Sci. Rep.* **2014**, *4*.
[71] J.-Y. Lee, S. T. Connor, Y. Cui, P. Peumans, *Nano Lett.* **2008**, *8*, 689.
[72] H. Lu, D. Zhang, X. Ren, J. Liu, W. C. H. Choy, *ACS Nano* **2014**, *8*, 10980.
[73] H. Lu, D. Zhang, J. Cheng, J. Liu, J. Mao, W. C. H. Choy, *Adv. Funct. Mater.* **2015**, *25*, 4211.
[74] T. H. Reilly, J. van de Lagemaat, R. C. Tenent, A. J. Morfa, K. L. Rowlen, *Appl. Phys. Lett.* **2008**, *92*, 243304.
[75] H. M. Stec, R. J. Williams, T. S. Jones, R. A. Hatton, *Adv. Funct. Mater.* **2011**, *21*, 1709.
[76] H. M. Stec, R. A. Hatton, *Adv. Energy Mater.* **2013**, *3*, 193.
[77] D. M. N. M. Dissanayake, B. Roberts, P.-C. Ku, *Appl. Phys. Lett.* **2011**, *99*, 113306.
[78] B. Niesen, B. P. Rand, P. Van Dorpe, D. Cheyns, L. Tong, A. Dmitriev, P. Heremans, *Adv. Energy Mater.* **2013**, *3*, 145.
[79] A. J. Smith, C. Wang, D. Guo, C. Sun, J. Huang, *Nat. Commun.* **2014**, *5*, 5517.
[80] A. Baba, N. Aoki, K. Shinbo, K. Kato, F. Kaneko, *ACS Appl. Mater. Interfaces* **2011**, *3*, 2080.
[81] B.-Y. Wang, T.-H. Yoo, J. W. Lim, B.-I. Sang, D.-S. Lim, W. K. Choi, D. K. Hwang, Y.-J. Oh, *Small* **2015**, *11*, 1905.
[82] J.-D. Chen, C. Cui, Y.-Q. Li, L. Zhou, Q.-D. Ou, C. Li, Y. Li, J.-X. Tang, *Adv. Mater.* **2015**, *27*, 1035.
[83] K. Kishino, M. S. Unlu, C. Jen-Inn, J. Reed, L. Arsenault, H. Morkoc, *IEEE J. Quantum Electron.* **1991**, *27*, 2025.
[84] M. S. Ünlü, S. Strite, *J. Appl. Phys.* **1995**, *78*, 607.
[85] Z. B. Wang, M. G. Helander, J. Qiu, D. P. Puzzo, M. T. Greiner, Z. M. Hudson, S. Wang, Z. W. Liu, Z. H. Lu, *Nat. Photon.* **2011**, *5*, 753.
[86] M. Agrawal, P. Peumans, *Opt. Express* **2008**, *16*, 5385.
[87] Y. Long, *Appl. Phys. Lett.* **2009**, *95*, 193301.
[88] Y. Long, *Appl. Phys. Lett.* **2011**, *98*, 033301.
[89] G. Kozyreff, D. C. Urbanek, L. T. Vuong, O. N. Silleras, J. Martorell, *Opt. Express* **2013**, *21*, A336.
[90] J. Lee, S.-Y. Kim, C. Kim, J.-J. Kim, *Appl. Phys. Lett.* **2010**, *97*, 083306.
[91] Y. Long, *Sol. Energy Mater. Sol. Cells* **2011**, *95*, 3400.
[92] E. Fortunato, D. Ginley, H. Hosono, D. C. Paine, *MRS Bull.* **2007**, *32*, 242.
[93] O. Inganas, *Nat. Photon.* **2011**, *5*, 201.
[94] W. Yu, X. Jia, Y. Long, L. Shen, Y. Liu, W. Guo, S. Ruan, *ACS Appl. Mater. Interfaces* **2015**, *7*, 9920.
[95] X. Ren, X. Li, W. C. H. Choy, *Nano Energy* **2015**, *17*, 187.
[96] K. Kushida, K. Hattori, S. Arai, T. Iimori, F. Komori, *Surf. Sci.* **1999**, *442*, 300.
[97] A. Anders, E. Byon, D.-H. Kim, K. Fukuda, S. H. N. Lim, *Solid State Commun.* **2006**, *140*, 225.
[98] S. G. Corcoran, G. S. Chakarova, K. Sieradzki, *Phys. Rev Lett.* **1993**, *71*, 1585.
[99] R. S. Sennett, G. D. Scott, *J. Opt. Soc. Am.* **1950**, *40*, 203.
[100] B. O'Connor, C. Haughn, K.-H. An, K. P. Pipe, M. Shtein, *Appl. Phys. Lett.* **2008**, *93*, 223304.
[101] V. J. Logeeswaran, N. P. Kobayashi, M. S. Islam, W. Wu, P. Chaturvedi, N. X. Fang, S. Y. Wang, R. S. Williams, *Nano Lett.* **2008**, *9*, 178.
[102] R. Koeppe, D. Hoeglinger, P. A. Troshin, R. N. Lyubovskaya, V. F. Razumov, N. S. Sariciftci, *ChemSusChem* **2009**, *2*, 309.
[103] S. Schubert, J. Meiss, L. Müller-Meskamp, K. Leo, *Adv. Energy Mater.* **2013**, *3*, 438.
[104] C. Tao, G. Xie, F. Meng, S. Ruan, W. Chen, *J. Phys. Chem. C* **2011**, *115*, 12611.
[105] L. Shen, Y. Xu, F. Meng, F. Li, S. Ruan, W. Chen, *Org. Electron.* **2011**, *12*, 1223.
[106] S. Schubert, M. Hermenau, J. Meiss, L. Müller-Meskamp, K. Leo, *Adv. Funct. Mater.* **2012**, *22*, 4993.
[107] L. Shen, S. Ruan, W. Guo, F. Meng, W. Chen, *Sol. Energy Mater. Sol. Cells* **2012**, *97*, 59.
[108] G. H. Jung, K. Hong, W. J. Dong, S. Kim, J.-L. Lee, *Adv. Energy Mater.* **2011**, *1*, 1023.
[109] L. Ke, S. C. Lai, H. Liu, C. K. N. Peh, B. Wang, J. H. Teng, *ACS Appl. Mater. Interfaces* **2012**, *4*, 1247.
[110] S. Kim, J.-L. Lee, *PHOTOE* **2012**, *2*, 021215.
[111] K. Hong, J. H. Son, S. Kim, B. H. Koo, J.-L. Lee, *Chem. Commun.* **2012**, *48*, 10606.
[112] C.-Z. Li, C.-C. Chueh, H.-L. Yip, F. Ding, X. Li, A. K. Y. Jen, *Adv. Mater.* **2013**, *25*, 2457.
[113] K.-S. Chen, H.-L. Yip, J.-F. Salinas, Y.-X. Xu, C.-C. Chueh, A. K. Y. Jen, *Adv. Mater.* **2014**, *26*, 3349.
[114] D. S. Ghosh, R. Betancur, T. L. Chen, V. Pruneri, J. Martorell, *Sol. Energy Mater. Sol. Cells* **2011**, *95*, 1228.
[115] W. Yu, L. Shen, F. Meng, Y. Long, S. Ruan, W. Chen, *Sol. Energy Mater. Sol. Cells* **2012**, *100*, 226.
[116] Y. Chen, L. Shen, W. Yu, Y. Long, W. Guo, W. Chen, S. Ruan, *Org. Electron.* **2014**, *15*, 1545.
[117] L. Shen, W. J. Yu, Y. B. Long, W. B. Guo, F. X. Meng, S. P. Ruan,, W. Y. Chen, *IEEE Electron Device Lett.* **2013**, *34*, 87.
[118] P. Shen, L. Shen, Y. B. Long, G. H. Chen, *IEEE Electron Device Lett.* **2014**, *35*, 1109.
[119] H. Jin, C. Tao, M. Velusamy, M. Aljada, Y. Zhang, M. Hambsch, P. L. Burn, P. Meredith, *Adv. Mater.* **2012**, *24*, 2572.
[120] W. Wang, M. Song, T.-S. Bae, Y. H. Park, Y.-C. Kang, S.-G. Lee, S.-Y. Kim, D. H. Kim, S. Lee, G. Min, G.-H. Lee, J.-W. Kang, J. Yun, *Adv. Funct. Mater.* **2014**, *24*, 1551.
[121] J. Zou, C.-Z. Li, C.-Y. Chang, H.-L. Yip, A. K. Y. Jen, *Adv. Mater.* **2014**, *26*, 3618.
[122] C.-C. Chueh, C.-Z. Li, A. K. Y. Jen, *Energy Environ. Sci.* **2015**, *8*, 1160.
[123] X. Guo, J. Lin, H. Chen, X. Zhang, Y. Fan, J. Luo, X. Liu, *J. Mater. Chem.* **2012**, *22*, 17176.
[124] Z. Xue, X. Liu, N. Zhang, H. Chen, X. Zheng, H. Wang, X. Guo, *ACS Appl. Mater. Interfaces* **2014**, *6*, 16403.
[125] J. Huang, C.-Z. Li, C.-C. Chueh, S.-Q. Liu, J.-S. Yu, A. K. Y. Jen, *Adv. Energy Mater.* **2015**, *5*, 1500406.
[126] C. J. An, C. Cho, J. K. Choi, J.-M. Park, M. L. Jin, J.-Y. Lee, H.-T. Jung, *Small* **2014**, *10*, 1278.
[127] C. J. An, H.-W. Yoo, C. Cho, J.-M. Park, J. K. Choi, M. L. Jin, J.-Y. Lee, H.-T. Jung, *J. Mater. Chem. A* **2014**, *2*, 2915.
[128] K. Yao, X.-K. Xin, C.-C. Chueh, K.-S. Chen, Y.-X. Xu, A. K. Y. Jen, *Adv. Funct. Mater.* **2015**, *25*, 567.
[129] Y.-E. Lee, S.-Y. Kim, W.-I. Jeong, J.-J. Kim, *Sol. Energy Mater. Sol. Cells* **2013**, *114*, 59.
[130] Y. Jin, J. Feng, M. Xu, X.-L. Zhang, L. Wang, Q.-D. Chen, H.-Y. Wang, H.-B. Sun, *Adv. Opt. Mater.* **2013**, *1*, 809.
[131] Y. Long, L. Shen, S. Ruan, W. Yu, Y. Wang, Q. Zeng, J. Luo, *Appl. Phys. Lett.* **2012**, *100*, 103304.
[132] L. Zuo, C.-Y. Chang, C.-C. Chueh, S. Zhang, H. Li, A. K. Y. Jen, H. Chen, *Energy Environ. Sci.* **2015**, *8*, 1712.
[133] L. Zuo, C.-C. Chueh, Y.-X. Xu, K.-S. Chen, Y. Zang, C.-Z. Li, H. Chen, A. K. Y. Jen, *Adv. Mater.* **2014**, *26*, 6778.
[134] M. E. Sykes, A. Barito, J. A. Amonoo, P. F. Green, M. Shtein, *Adv. Energy Mater.* **2014**, *4*, 1301937.
[135] F. Pastorelli, P. Romero-Gomez, R. Betancur, A. Martinez-Otero, P. Mantilla-Perez, N. Bonod, J. Martorell, *Adv. Energy Mater.* **2015**, *5*, 1400614.
[136] Y.-H. Chen, C.-W. Chen, Z.-Y. Huang, W.-C. Lin, L.-Y. Lin, F. Lin, K.-T. Wong, H.-W. Lin, *Adv. Mater.* **2014**, *26*, 1129.